Autism-associated 16p11.2 microdeletion impairs prefrontal functional connectivity in mouse and human

Alice Bertero[1,2*] PhD, Adam Liska[1*] PhD, Marco Pagani[1*] PhD, Roberta Parolisi[3] PhD, Maria Esteban Masferrer[4] PhD, Marta Gritti[5] PhD, Matteo Pedrazzoli[5] MSc, Alberto Galbusera[1] MSc, Alessia Sarica[7] PhD, Antonio Cerasa[7,8] PhD, Mario Buffelli[6] PhD, Raffaella Tonini[5] PhD, Annalisa Buffo[3] PhD, Cornelius Gross[4] PhD, Massimo Pasqualetti[2,1] PhD, Alessandro Gozzi[1] PhD

[1]Functional Neuroimaging Laboratory, Center for Neuroscience and Cognitive Systems @UniTn, Rovereto, Italy

[2]Department of Biology, Unit of Cell and Developmental Biology, University of Pisa, Pisa, Italy

[3]Department of Neuroscience Rita Levi-Montalcini - University of Torino, Neuroscience Institute Cavalieri Ottolenghi (NICO), Torino, Italy

[4]Epigenetics & Neurobiology Unit, European Molecular Biology Laboratory (EMBL), Monterotondo, Italy

[5]Neuroscience and Brain Technologies Department, Istituto Italiano di Tecnologia, Genova, Italy

[6]Department of Neurosciences, Biomedicine and Movement Sciences, University of Verona, Italy

[7]Consiglio Nazionale delle Ricerche, Catanzaro, Italy

[8]S. Anna Institute and Research in Advanced Neuro-rehabilitation (RAN) Crotone, Italy

*Equal first author contribution

Corresponding author
Alessandro Gozzi
Functional Neuroimaging Laboratory,
Center for Neuroscience and Cognitive Systems @ UniTn,
Istituto Italiano di Tecnologia,
38068, Rovereto, Italy
alessandro.gozzi@iit.it

Running title: Impaired frontal connectivity in 16p11.2 deletion

Abstract

Human genetic studies are rapidly identifying variants that increase risk for neurodevelopmental disorders. However, it remains unclear how specific mutations impact brain function and contribute to neuropsychiatric risk. Chromosome 16p11.2 deletion is one of the most common copy number variations in autism and related neurodevelopmental disorders. Using resting-state functional magnetic resonance imaging data from the Simons VIP database, we show that 16p11.2 deletion carriers exhibit impaired prefrontal connectivity, resulting in weaker long-range functional coupling with temporal-parietal regions. These functional changes are associated with socio-cognitive impairments. We also document that a mouse with the same genetic deficiency exhibits similarly diminished prefrontal connectivity, together with thalamo-prefrontal miswiring and reduced long-range functional synchronization. These results reveal a mechanistic link between specific genetic risk for neurodevelopmental disorders and long-range functional coupling, and suggest that deletion in 16p11.2 may led to impaired socio-cognitive function via dysregulation of prefrontal connectivity.

Keywords: fMRI, DMN, resting-state, thalamus, imaging

Introduction

Over the past decade significant strides have been made toward understanding the genetic basis of autism spectrum disorders (ASD) and related heritable neurodevelopmental conditions (Chen *et al.*, 2015; Tick *et al.*, 2016). The identification of several gene variants and mutations associated with increased ASD risk (de la Torre-Ubieta *et al.*, 2016) has advanced our understanding of ASD mechanisms, by providing a platform for unravelling the causal chain of events that result in ASD. However, great challenges remain in delineating how heterogeneous genetic forms of ASD might converge into circuital and behavioral alterations characteristic of this cluster of disorders.

Chromosomal copy number variations (CNVs) have been associated with 5-10% of ASD patients (de la Torre-Ubieta *et al.*, 2016). Microdeletion of human chromosome 16p11.2 is one of the most common CNVs in ASD, accounting for approximately 0.5 to 1% of all cases (Kumar *et al.*, 2008; Malhotra and Sebat, 2012). The affected region encompasses ~29 annotated protein-coding genes, many of which are expressed in the brain (Blumenthal *et al.*, 2014). Previous studies have demonstrated that ASD is diagnosed in approximately 18% of 16p11.2 deletion carriers and that this CNV affects global cognition by resulting in a highly penetrant reduction in intelligence quotient (IQ, Zufferey *et al.*, 2012). Importantly, human neuroimaging investigations in children with the 16p11.2 deletion have revealed brain structural abnormalities affecting gray matter areas previously implicated in ASD (Qureshi *et al.*, 2014; Maillard *et al.*, 2015). Deletion in syntenic regions to 16p11.2 in animals results in neural apoptosis deficits and increased neuronal progenitor proliferation (Golzio *et al.*, 2012; Pucilowska *et al.*, 2015),

suggesting a role of precocious molecular and cellular events in the establishment of deviant brain morphoanatomy associated with 16p11.2 deletion. However, it remains unclear whether and how these neuroanatomical alterations affect brain function, and what brain substrates are primarily affected.

Mounting evidence points at a role for aberrant functional connectivity in the resting state as a hallmark feature of ASD (Di Martino *et al.*, 2013). However, great heterogeneity exists in the manifestation of abnormal connectivity across studies and, besides a few notable exceptions (Scott-Van Zeeland *et al.*, 2010; Rudie *et al.*, 2012), attempts to relate individual ASD genetic etiologies to specific connectional or circuital dysfunctions have been lacking. In the present work we mapped functional connectivity in a genetically defined cohort of 16p11.2 deletion carriers (Simons VIP Consortium, 2012) as assessed with resting state functional magnetic resonance imaging (rsfMRI). We show that 16p11.2 deletion impairs prefrontal functional connectivity, resulting in reduced global connectivity and impaired long-range coupling in parieto-temporal associative regions of the default mode network. We corroborate these findings in a mouse model of 16p11.2 deletion (Horev *et al.*, 2011), in which we observed similarly reduced long-range prefrontal connectivity, as well as thalamo-prefrontal miswiring and reduced low-frequency neuronal synchronization. Our results in mouse and human suggest that deletion in 16p11.2 may lead to impaired cognition and ASD-like symptoms via dysregulation of long-range prefrontal functional synchronization.

Material and methods

Full-length experimental procedures can be found in Supplemental Information.

Ethical Statement

All study procedures were approved by the institutional review board at the involved medical centers and are in accordance with the ethical standards of the Helsinki Declaration of 1975, as revised in 2008. Animals studies were conducted in accordance with the Italian Law (DL 26/214, EU 63/2010, Ministero della Sanità, Roma) and the recommendations in the Guide for the Care and Use of Laboratory Animals of the National Institutes of Health. Animal research protocols were also reviewed and consented to by the animal care committee. All surgical procedures were performed under deep anesthesia.

Human rsfMRI

rsfMRI mapping focused on initially identified probands and their siblings with deletion at 16p11.2 as part of a multi-center investigation (Simons VIP Consortium, 2012). MR imaging was performed on 3T Tim MR scanners with TR = 3000 ms, TE = 30 ms, 124 repetitions for a total scan time of 6'12''. A final list of 19 and pediatric deletion carriers (age 8–16 years; 10 males and 9 females) and 28 pediatric controls (age 7–16 years; 16 males and 12 females) were included in the study. A breakdown of subject demographics is reported in Table I and Supplemental Table 1. Image preprocessing was based on previous studies of the ABIDE dataset (Di Martino *et al.*, 2013) and on the Preprocessed Connectomes Project. To control for motion contamination, we

removed all frames whose frame-wise displacement was larger than 0.5mm (Power *et al.*, 2012; Di Martino *et al.*, 2013) and we only retained subjects in which > 80% of rsfMRI volumes were retained. The number of scrubbed volumes and mean frame-wise displacement for each subject are reported in Supplementary Table 2. The whole pre-processing pipeline was implemented using the Configurable Pipeline for the Analysis of Connectomes (C-PAC v1.0.1a).

Network centrality was mapped as implemented in C-PAC (Di Martino *et al.*, 2013). To map intergroup differences in connectivity we applied a multiple regression model (covariates: age, gender, group-centered NVIQ, site, and mean frame-wise displacement) and used a *t*-test to assess the statistical significance of the regression coefficient corresponding to the group variable ($P < 0.05$, family-wise error corrected, with cluster-defining threshold of $t_{40} > 2.01$, $p < 0.05$ as implemented in FSL). We subsequently performed a seed-based analysis using a seed in the medial prefrontal area exhibiting significantly-reduced centrality in the 16p11.2 deletion group (Figure 1A), using a multiple regression model as above. Linear Discriminant Analysis (LDA) was performed using MASS library v7.3 (Ripley, 2015).

Mouse Studies

Functional and structural MRI

rsfMRI experiments were performed on male adult 16p11.2$^{+/-}$ mice and wild-type littermates (n = 12 and n = 11, respectively) using halothane-induced sedation. Animal preparation has been recently described in greater detail (Ferrari *et al.*, 2012; Sforazzini *et al.*, 2014). Intergroup differences in functional connectivity were mapped using

network centrality and seed-based mapping to recapitulate the approach applied to human imaging data (Liska *et al.*, 2015; Liska *et al.*, 2017). Diffusion-weighted (DW) MRI was carried out on the same subjects employed for rsfMRI mapping in paraformaldehyde fixed specimens as previously described (Dodero *et al.*, 2013). Brains were imaged inside intact skulls to avoid post-extraction deformations. MR tractography was carried out as previously described (Liska *et al.*, 2017). To qualitatively compare white matter microstructural parameters in humans and mice, we mapped fractional anisotropy using Tract-Based Spatial Statistics (TBSS) analysis, as implemented in FSL (Dodero *et al.*, 2013).

In-vivo Electrophysiology

Experiments were performed on 16p11.2$^{+/-}$ and control littermates (n = 6, each group) as previously described (Zhan *et al.*, 2014) using two electrodes placed in the prefrontal and retrosplenial cortex. Local field potential (LFP) recordings were carried out under halothane sedation to reproduce the conditions of rsfMRI imaging.

Retrograde Viral Tracing with Rabies Virus

Unpseudotyped recombinant SADΔG-mCherry rabies virus (RV) was produced as described in Fumitaka and Callaway (2013). Prefrontal rabies virus injections were carried out and quantified as previously described (Sforazzini *et al.*, 2014) in adult male 16p11.2$^{+/-}$ and control 16p11.2$^{+/+}$ littermates (*n* = 6, each group).

Dendritic Spine Analysis

Experiments were performed on adult control and 16p11.2$^{+/-}$ mice (N = 8, each group). We quantified the density of dendritic spines in the anterior cingulate cortex and

somatosensory cortex using the Golgi-Cox staining method as recently described (Martino *et al.*, 2013).

Brain Slice Electrophysiology

Brain slice electrophysiology was carried out as recently described (Giorgi *et al.*, 2017) on young adult 16p11.2$^{+/+}$ and 16p11.2$^{+/-}$ mice (12 week old, n = 4 per group). Whole-cell patch-clamp recordings were made on pyramidal neurons of the layer V of the prefrontal cortex. Spontaneous excitatory post-synaptic currents (sEPSCs) were recorded in presence of 10 μM Gabazine. For miniature EPSCs (mEPSCs), recordings were made also in presence of 1 μM TTX.

Electron Microscopy

Conventional electron microscopy was carried out as described in (Zhan *et al.*, 2014), using adult 16p11.2$^{+/-}$ (n = 4) and control littermate (n = 3) mice.

Results

Reduced prefrontal connectivity in 16p11.2 deletion carriers

To investigate whether 16p11.2 deletion affects brain functional connectivity, we mapped resting-state fMRI connectivity in human children with 16p11.2 deletion and control subjects (n = 19, and n=28, respectively, Simons VIP consortium, 2012). In keeping with prior investigations in the same patient cohort (Owen *et al.*, 2014), full scale and non-verbal IQ were significantly lower, while social responsiveness score was higher in deletion carriers with respect to control subjects (t_{44} = 3.47, p = 0.001; t_{45} = 2.83, p = 0.007; t_{45} = 7.78, p < 0.001, respectively, *t*-test). Demographics and diagnosis are reported in Table 1 and Supplementary Table 1, respectively.

To obtain a spatially unbiased assessment of brain-wide functional connectivity, we mapped whole-brain global connectivity differences across the two cohorts. The metric employed, also referred to as weighted degree centrality (Cole *et al.*, 2010; Rubinov and Sporns, 2011), is a good predictor of higher socio-cognitive performance (Cole *et al.*, 2012) and a sensitive marker of network dysfunction in brain connectopathies (Cole *et al.*, 2011; Di Martino *et al.*, 2013; Supekar *et al.*, 2013; Cheng *et al.*, 2015b). Whole-brain voxel-wise mapping revealed reduced global connectivity in the medial prefrontal cortex (PFC) of 16p11.2 deletion carriers (Figure 1A, p < 0.05, family-wise corrected with a cluster-defining threshold t_{40} > 2.01). We also observed foci of reduced connectivity in temporal and parietal areas involved in socio-cognitive functioning, such as the superior and medial temporal gyrus, and temporal-parietal junctions (Figure 1A).

To map the target regions underlying the identified connectivity reduction, we probed whole-brain functional connectivity using a seed region placed in the affected medial prefrontal area (Figure 1B). We chose the PFC because of its key involvement in social cognition and higher cognitive functions (Blakemore, 2008; Cole *et al.*, 2012; Grossmann, 2013), two domains that are impaired in 16p11.2 deletion carriers (Zufferey *et al.*, 2012). This analysis revealed the presence of reduced long-range connectivity with the PFC in multiple areas of 16p11.2 deletion carriers (Figure 1B). Prominent connectivity reductions were observed in the latero-temporal cortex, and inferior parietal lobule, two associative regions of the default mode network, as well as in the superior and inferior frontal cortex and paracentral gyrus ($p < 0.05$, family-wise corrected, with cluster-defining threshold of $t_{40} > 2.01$). A similar pattern of hypoconnectivity was obtained when NVIQ was not used as covariate in the regression model (Supplementary Figure 1). These findings reveal the presence of reduced long-range functional connectivity in the medial prefrontal cortex of human 16p11.2 deletion carriers.

PFC connectivity strength exhibited strong inverse correlation with social responsiveness scale (SRS) score ($r = -0.52$, $p < 0.001$, $n = 47$, Figure 1C). To investigate the combined predictive power of SRS score and PFC connectivity strength on CNV status, we used a linear discriminant analysis (Figure 1D). We found that PFC connectivity strength alone leads to a correct classification of CNV status in 24/28 of controls (specificity = 85.7%) and 13/19 deletion subjects (sensitivity = 68.4%), with an overall accuracy of 37/47 (78.7%). SRS scores *per se* exhibited higher predictive value, leading to a correct classification of 28/28 controls (specificity = 100%) and 15/19

deletion subjects (sensitivity = 78.9%) with an overall accuracy of 43/47 (91.5%). The combined use of PFC connectivity strength and SRS scores did not improve prediction of CNV status, leading to the same specificity, sensitivity and accuracy obtained with SRS score alone. PFC connectivity strength was also moderately correlated with FSIQ and NVIQ ($r = 0.47$, $p = 0.001$, and $r = 0.38$, $p = 0.009$, respectively, $n = 47$, Supplementary Figure 2).

Reduced prefrontal connectivity and neural synchronization in a mouse model of 16p11.2 deletion

To corroborate the human findings and bolster a role of 16p11.2 deletion in affecting prefrontal connectivity, we used resting-state fMRI to map functional connectivity in a mouse line harboring a deletion in orthologous regions to human 16p11.2 (Horev *et al.*, 2011) under light sedation. The imaging approach employed permits to probe large-scale network organization in rodents (Gozzi and Schwarz, 2015) and is highly sensitive to genetic and developmental modulation of macroscale connectivity (Sforazzini *et al.*, 2014; Liska *et al.*, 2017). Based on human findings we hypothesized that similar prefrontal long-range connectivity impairments could be identified in 16p11.2$^{+/-}$ mice. To test this hypothesis, we first mapped whole-brain global connectivity differences between 16p11.2 mutant mice and control littermates using the same connectivity metric employed for human mapping (weighted degree centrality, Liska *et al.*, 2015). The approach revealed a focal reduction in global connectivity in the medial prefrontal cortex of 16p11.2$^{+/-}$ mutant mice (Figure 2A, $p < 0.05$, cluster-defining threshold $t_{21} > 2.08$), consistent with the global connectivity differences observed in human 16p11.2 deletion carriers. To probe the long-range substrates affected by the identified prefrontal

hypoconnectivity, we next carried out seed-based mapping using a seed centered in the PFC. This analysis revealed a significant connectivity reduction in posterior parietal and retrosplenial cortices (Fig. 2B, $p < 0.05$, cluster-defining threshold $t_{21} > 2.08$), two associative regions of the mouse default mode network involved in sensory integration (Robinson *et al.*, 2014; Gozzi and Schwarz, 2015; Whitlock, 2017). Foci of reduced connectivity were also observed in the medial-dorsal thalamus. To further probe the presence of long-range functional coupling with the prefrontal cortex in 16p11.2 mutants, we carried out a seed-based quantification of prefrontal connectivity across midline cortical regions of the mouse brain. This analysis revealed a significant reduction in long-rage connectivity in 16p11.2$^{+/-}$ mice along the rostro-caudal axis of the cingulate and retrosplenial cortex (repeated measures two-way ANOVA, genotype-effect: $F_{1,21} = 5.70$, $p = 0.027$, Figure 2C-D). Inter-hemispheric connectivity in subcortical or motor-sensory rsfMRI networks appeared to be otherwise preserved (Supplementary Figure 3).

To corroborate a neural origin for the observed connectivity reduction, we carried out local field potential (LFP) coherence measurements in a separate cohort of mice under the same experimental conditions used in our imaging studies. We probed the presence of long-range connectivity deficits by placing electrodes in the prefrontal and retrosplenial cortex, two regions characterize by reduced functional coupling in 16p11.2 mutants as assessed with rsfMRI. These measurements highlighted reduced long-range low-frequency LFP coherence in 16p11.2$^{+/-}$ mice, resulting in a robust genotype x frequency interaction ($F_{156,1560} = 2.29$, $p < 0.001$, Figure 2E) and a reduction in the delta frequency power (t-test, $t_{10} = 3.73$, $p = 0.007$, $q_{FDR} = 0.028$, Figure 2F), a rhythmic

activity that is strongly correlated with spontaneous fMRI fluctuations (Lu *et al.*, 2007). These findings suggest that 16p11.2 deletion can reduce long-range prefrontal coupling via impaired low-frequency synchronization.

Importantly, we did not observe genotype-dependent differences in anesthesia sensitivity as measured with arterial blood pressure mapping (t-test, $t_{21} = 0.96$, $p = 0.35$; Supplementary Figure 4) or amplitude of cortical BOLD signal fluctuations (t-test, $t_{21} = 0.16$, $p = 0.87$, Supplementary Figure 4), two independent readouts linearly correlated with anesthesia depth (Steffey *et al.*, 2003; Liu *et al.*, 2011). Minimal alveolar concentration, another measure of anesthesia sensitivity, was also comparable across experimental groups (1.31 ± 0.08 % and 1.34 ± 0.09%, respectively, $p = 0.48$, Kolmogorov-Smirnov test). These results argue against a confounding contribution of the anesthetic to the observed connectivity impairments in 16p11.2$^{+/-}$ mice.

Altered thalamo-prefrontal wiring in 16p11.2$^{+/-}$ deletion mice

To probe a contribution of *macroscopic* white matter rearrangement to the observed functional hypoconnectivity, we carried out MRI tractography analysis of the corpus callosum, cingulum and anterior commissure, three major white matter tracts characterized by extensive cortico-cortical, antero-posterior extension. We found these white matter bundles to be largely typical in mutant and control mice (Figure 3A). Fiber streamline quantifications did not reveal any genotype dependent differences in the number of streamlines (cingulum: $t_{23} = 1.51$, $p = 0.14$; corpus callosum: $t_{23} = 1.45$, $p = 0.16$; Supplementary Figure 5). These results rule out a contribution of gross macroscale white matter alterations to the observed functional hypoconnectivity.

To examine the presence of finer-scale wiring alterations undetectable by tractography, we carried out monosynaptic retrograde tracing of the left prefrontal cortex in 16p1.2$^{+/-}$ mice. Besides being a key cortical substrates affected by 16p11.2 deletion, this region also receives widespread innervation by the thalamus (Hoover and Vertes, 2007; Liska *et al.*, 2017), an anatomical substrate involved in the generation of delta activity (McCormick and Pape, 1990). This characteristic offers the opportunity to establish a putative link between mesoscale connectional alterations and the observed reduction in functional connectivity. Quantification of the relative fraction of labelled cells revealed the presence increased projection frequency in the mediodorsal thalamus of 16p11.2$^{+/-}$ mice (t_{10} = 4.55, p = 0.001, FDR corrected, Figure 3B-C), a region exhibiting reduced rsfMRI synchronization with the PFC (Fig. 2B). No genotype-dependent difference in the frequency of prefrontal projecting neurons was observed in any of the other cortical or subcortical regions examined (Figure 3C).

Because altered long-range projection input may affect synaptic input and dendritic spine density in target regions (Glausier and Lewis, 2013), we also quantified dendritic spine density in cortical layers 2/3 in dysfunctional (PFC) and unaffected (somatosensory) cortical areas of 16p11.2$^{+/-}$ mice. Interestingly, we observed a significant reduction in dendritic spine density in the PFC, but not in the somatosensory cortex of 16p11.2$^{+/-}$ mice (t_{15} = 5.11, p = 0.00012, FDR corrected, Supplementary Figure 6A). These results corroborate the regional specificity of the observed functional impairments, and suggest a possible contribution of synaptic deficits to the prefrontal impairment observed in 16p11.2 deletion. Whole-cell patch clamp electrophysiological recordings in prefrontal pyramidal neurons of 16p11.2$^{+/-}$ mice did not reveal genotype-

dependent differences in spontaneous and miniature excitatory post synaptic currents (Supplementary Figure 6B-E).

Widespread white matter microstructure alterations in 16p11.2$^{+/-}$ mice

We finally examined the presence of *microscale* white matter structural abnormalities in 16p11.2$^{+/-}$ mutants via MR-based measurements of fractional anisotropy, a marker of microstructural integrity that has been recently described to be altered in the same patient cohort examined here (Owen *et al.*, 2014; Chang *et al.*, 2016). In keeping with human findings, we found widespread increase in fractional anisotropy in major white matter tracts of 16p11.2$^{+/-}$ mice ($p < 0.05$, corrected with threshold-free cluster enhancement, Figure 4A and C; $t_{23} = 2.48$, $p = 0.021$), suggesting that 16p11.2 deletion similarly affects white matter microstructure in humans and rodents. By using electron microscopy, we identified increased axonal diameter in callosal fibers as a plausible cellular correlate of these alterations (Figure 4B). Specifically, we found callosal neurons to have thicker myelin ($t_{446} = 2.7$, $p = 0.007$, Figure 4C), larger diameter ($t_{348} = 2.498$, $p = 0.012$, Figure 4C) and a higher g ratio ($t_{446} = 2.58$, $p = 0.010$, Figure 4C) in 16p11.2$^{+/-}$ mice with respect to control littermates. In contrast with the more focal functional impairments observed in 16p11.2 deletion carriers and in the mouse model, the microstructural alteration appeared to be widespread and as such are unlikely to represent a direct correlate of the observed functional hypoconnectivity.

Discussion

Here we show that 16p11.2 deletion results in reduced prefrontal connectivity and impaired long-range functional coupling with temporal-parietal regions. We also document that a mouse line with the same genetic deficiency exhibits similarly diminished reduced prefrontal connectivity, together with thalamo-prefrontal miswiring and reduced long-range low-frequency neural synchronization. These findings establish a link between a common ASD-associated CNV and impaired macroscale connectivity, suggesting that 16p11.2 deletion can predispose to neurodevelopmental disorders and impaired socio-cognitive function via a dysregulation of long-range prefrontal synchronization. The paradigm used here—in which functional neuroimaging across species is used to explore the functional consequences of a known disease-associated variant in a highly focused manner—is likely to be of widespread utility in the elucidation of the mechanisms underlying the functional disconnectivity associated with disorders of human cognition and development.

The observed connectivity impairments add to an increasing body of experimental work pointing at the presence of aberrant functional synchronization in ASD and severe developmental disorders. While largely heterogeneous in its manifestation, brain-wide functional connectivity has been reported to be largely disrupted in autistic patients (Vasa *et al.*, 2016; Hull *et al.*, 2017). Our results underscore a contribution of impaired long-range functional synchronization as a key predisposing factor of cognitive and social impairments associated with 16p11.2 deletion. The involvement of prefrontal areas as well as associative regions of the default mode network is consistent with prior rsfMRI studies which have reported this network as being particularly vulnerable in ASD

(Di Martino *et al.*, 2013; Washington *et al.*, 2014). As brain maturation is reflected in strengthening of long-range cortical-cortical connectivity (Dosenbach *et al.*, 2010) the observed functional impairments could be indicative of a delayed or immature connectivity between higher-order integrative regions. According to this view, the involvement of prefrontal regions may reflect the especially slow maturation of these substrates, a process that continues up to adulthood (Sowell *et al.*, 1999).The reduced connectivity observed in temporal-parietal areas and in associative regions of the default mode network is also equally noteworthy, owing to the implication of these areas in socio-cognitive functions that are impaired in 16p11.2 deletion carriers and ASD patients (Bernhardt *et al.*, 2014; Cheng *et al.*, 2015a; Hanson *et al.*, 2015). The fact that the observed connectional impairments are not strictly dependent on a specific diagnosis suggests that this CNV mediates risk by modulating the continuum of normal brain function, as would be expected for intermediate phenotypes related to cognition and behavior (Scott-Van Zeeland *et al.*, 2010; Rudie *et al.*, 2012).

The presence of reduced prefrontal connectivity in a mouse line recapitulating human 16p11.2 deletion underscores the involvement of prefrontal integrative regions as a key macroscale substrate of this genetic deficiency, and offers the possibility of generating hypotheses about possible neural mechanisms underlying this impairment. A macroscale investigation of white matter connectivity using DTI ruled out the presence of major structural rearrangements in 16p11.2 mutants. However, functional connectivity alterations are rarely a direct proxy of underlying white matter reorganization (Anagnostou and Taylor, 2011), and remarkable examples of dissociation between macroscopic anatomical organization and functional connectivity have been described

in humans (Tyszka *et al.*, 2011; Paul *et al.*, 2014). The observation of increased thalamo-frontal wiring and functional dysconnectivity in 16p11.2$^{+/-}$ mutants points at the involvement of *mesoscopic* alterations in long-range projecting populations as a putative driver of this endo-phenotype, possibly the result of abnormal synaptic refinement or circuit maturation during early development (Zhan *et al.*, 2014; Riccomagno and Kolodkin, 2015). As 16p11.2$^{+/-}$ mice exhibit altered cortical progenitor proliferation and increased density of cortico-thalamic projecting neurons (Pucilowska *et al.*, 2015), this abnormality could reflect defective cortical feedback, leading to compromised feedforward refinement of thalamo-prefrontal projections (Thompson *et al.*, 2016) and *increased* synaptic multiplicity, a neural phenotype associated with autism-like behavior and *reduced* functional connectivity in the mouse (Zhan *et al.*, 2014). The observation of impaired delta rhythms in 16p11.2 mutant mice is broadly consistent with this hypothesis, given the key involvement of thalamic relay neurons in the generation of delta activity (McCormick and Pape, 1990). The presence of altered spine density in prefrontal but not motor-sensory areas of 16p11.2$^{+/-}$ mice corroborates the regional specificity of the network alterations observed, and provides additional mechanistic clues as to the observed functional impairments. Because thalamo-cortical inputs represent a limited proportion of all glutamatergic synapses in the cortex (Peters, 2002), a decreased spine density may reflect maturational deficits affecting microscale cortico-cortical connectivity. A number of additional neurophysiological mechanisms could also play a role in the generation of neural desynchronization and reduced functional connectivity, including altered inhibitory/excitatory activity, a feature associated with several autism-related mutations (Marín, 2012) and resulting in inefficient long-range

synchronization (Cardin *et al.*, 2009). By contrast, the widespread increase in white matter fractional anisotropy observed in 16p11.2$^{+/-}$ mice represents an unlikely correlate of the observed network alterations, given its widespread distribution and lack of pathway specificity. The correspondence with analogous fractional anisotropy mapping in human 16p11.2 carriers (Owen *et al.*, 2014; Chang *et al.*, 2016) is however of interest *per se,* as it represents an intrinsic corroboration of the translational validity of the mouse model employed as far as white matter microstructure is concerned.

Despite the considerable evolutionary distance between rodents and humans, our direct comparison of orthologous 16p11.2 mutations revealed broadly similar prefrontal functional hypoconnectivity across-species, as well as reduced long-range rsfMRI coupling between prefrontal and long-range associative cortical areas. Discrepancies in the location of these effects were also noted, such as the observation of reduced retrosplenial and thalamic connectivity in mouse but not human 16p11.2 deletion carriers, and a larger involvement of latero-cortical regions in the clinical cohort. Evolutionary differences in the organization and extension of prefrontal and associative cortices can plausibly account for some of these discrepancies. Postero-parietal associative areas in rodents are disproportionately smaller than their primate counterparts (Whitlock, 2017), and rodents lack regions cyto-architecturally homologous to the human ventral or dorsolateral PFC, or the precuneus (Vogt and Paxinos, 2014; Carlén, 2017). These divergences are consistent with a more focal involvement of parieto-cortical areas in 16p11.2 mutant mice. Moreover, thalamo-frontal functional coupling in rodents is considerably stronger than in humans, as documented by the involvement of thalamic areas as core constituents of the rodent, but not human, default

mode network (Gozzi and Schwarz, 2015; Cunningham *et al.*, 2017). A stronger thalamo-frontal synchronization in rodent may explain the different thalamic involvement observed in this study. By contrast, the lack of retrosplenial/precuneal hypoconnectivity in human 16p11.2 deletion carriers cannot be straightforwardly accounted for in evolutionary terms, given the comparably strong coupling of these areas with prefrontal cortex in both species (Gozzi and Schwarz, 2015). However, cross-species differences in the topology, organization and connectivity of these areas exist, the most notable of which being an antero-posterior shift of these areas as high-centrality integrative "network hubs", ranging from prefrontal substrates in rodent to precuneal and posterior midline regions in primate and human (Liska *et al.*, 2015). Finally, additional experimental (e.g. anesthesia) and biological differences could contribute to the observed spatial discrepancies, including species-specific neuroadaptive or compensatory mechanisms secondary to 16p11.2 deletion, and the impossibility to fully and closely replicate experimental conditions across species as a result of technical or procedural constraints.

Using the same imaging paradigm employed here, we recently identified impaired prefrontal connectivity in mice harboring mutations in autism-risk gene CNTNAP2 (Liska *et al.*, 2017), an effect that recapitulates analogous observations in human carriers of CNTNAP2 polymorphisms (Scott-Van Zeeland *et al.*, 2010). Prefrontal reductions in connectivity has also been reported in other mouse lines recapitulating autism-associated risk factors such as callosal agenesis (Sforazzini *et al.*, 2014), or genetic mutations involving cell adhesion or synaptic scaffolding genes (Michetti *et al.*, 2017; Pagani *et al.*, 2017). These correspondences suggest that

impaired prefrontal connectivity could underlie core cognitive and behavioral deficits shared by a multiple autism-associated genetic etiologies. Prefrontal aberrancies are however unlikely to represent a single unifying mechanism in autism, as opposing functional alterations have been reported in human studies (Hull *et al.*, 2017) and are also emerging in mouse imaging studies. For example, mice harboring a mutation in autism-associated gene ChD8 show *increased* functional connectivity in hippocampal and sensory regions (Suetterlin *et al.*, 2017). By extending this investigational paradigm to multiple ASD-related risk factors it will be possible to identify shared connectional signatures, and formally probe a contribution of genetic variability to the heterogeneous expression of functional dysconnectivity in patient populations.

From a methodological standpoint, our rsfMRI results are bolstered by their recapitulation in two species, but also by a link to clinical symptoms revealing more severe socio-cognitive deficits in children exhibiting greater reductions in prefrontal functional connectivity. A confounding contribution of motion-related artefacts (Power *et al.*, 2015) to our human findings is highly unlikely, because we found overall motion to be comparable across groups, we used the 'scrubbing' method at a motion threshold used for rsfMRI connectivity assessment in prominent clinical ASD databases (0.5 mm, Di Martino *et al.*, 2013; Falahpour *et al.*, 2016; Balsters *et al.*, 2017) and we also conservatively analyzed only subjects in which censoring permitted to retain > 80% of the original timeseries. We also regressed mean framewise displacement as a covariate of no interest. Although stricter motion censoring has been proposed (e.g. 0.2 mm, (Supekar *et al.*, 2013)) this threshold did not permit to retain a sufficient number of subjects for statistical mapping in this study. We therefore resorted to replicate these

measurements in the mouse, in which the use of sedation and mechanical ventilation results in negligible motion contamination(Ferrari *et al.*, 2012). Collectively, our findings strongly argue against a confounding role of motion in the impaired prefrontal connectivity observed in 16p11.2 deletion carriers.

In conclusion, here we document that 16p11.2 deletion leads to impaired prefrontal functional connectivity in mouse and human, an effect associated with aberrant fronto-thalamic wiring and long-range neural desynchronization. Our findings suggest that 16p11.2 deletion may predispose to neurodevelopmental disorders and autism through selective dysregulation of connectivity in integrative prefrontal areas, and provide a translational model for investigating connectional perturbations associated with syndromic developmental disorders.

Acknowledgments

We are grateful to all of the families at the participating Simons Variation in Individuals Project (Simons VIP) sites and the Simons VIP Consortium. We appreciate obtaining access to phenotypic, genetic and imaging data on SFARI Base. Approved researchers can obtain the Simons VIP population dataset described in this study by applying at https://base.sfari.org.

Funding

The study was funded by grants from the Simons Foundation (SFARI 314688 and 400101, A. Gozzi). A. Gozzi also acknowledges funding from the Brain and Behavior Foundation (2017 NARSAD independent Investigator Grant).

Conflict of interests

The authors declare that they have no conflict of interest.

Legends to Supplemental Figures

Supplementary Figure 1 – Functional connectivity mapping without NVIQ covariate.

(A) Global connectivity mapping and (B) target regions of long-range prefrontal hypoconnectivity in 16p11.2 deletion carriers with respect to typically developing (TD) control subjects. The spatial distribution of the effect is very similar to that depicted in Figure 1A, in which connectivity mapping was carried out using NVIQ as a covariate.

Supplementary Figure 2 - Correlation between prefrontal connectivity and IQ metrics in human 16p11.2 deletion carriers.

Correlation between PFC connectivity and NVIQ (left), or FSIQ (right) in the experimental cohort examined ($r = 0.466$, $p = 0.001$, and $r = 0.376$, $p = 0.009$, respectively, $n = 47$).

Supplementary Figure 3 - Largely preserved inter-hemispheric connectivity in 16p11.2$^{+/-}$ mice

Correlation coefficients were calculated between time courses extracted from the volumes of interest depicted on the right, and the resulting r-scores were transformed to z-scores using Fisher's r-to-z transform. None of these comparisons survived a false discovery rate correction at $q = 0.05$.). All data are means ± SEM. Au: auditory cortex, CPu: caudate-putamen, Ins: insular cortex, M1: primary motor cortex, S1: somatosensory cortex, V1: primary visual cortex.

Supplementary Figure 4 - Comparable sensitivity to anesthesia in 16p11.2$^{+/-}$ and control mice

We did not observe genotype-dependent differences in anesthesia sensitivity as measured with arterial blood pressure mapping (t_{21} = 0.96, p = 0.35) and amplitude of cortical BOLD signal fluctuations in primary motor cortex (t_{21} = 0.16, p = 0.87). All data are means ± SEM. M1: primary motor cortex.

Supplementary Figure 5 – Largely-preserved macroscale white-matter connectivity in 16p11.2$^{+/-}$ mice.

Fractional group fiber density maps for corpus callosum and cingulum tracts (16p11.2$^{+/+}$ left, 16p11.2$^{+/-}$ right). (B) White-matter tractography-based streamline counts. Numbers of streamlines in corpus callosum and cingulum did not show any significant inter-group difference between 16p11.2$^{+/-}$ mice and control littermates (cingulum: *t*-test, t_{23} = 1.51, p = 0.14; corpus callosum: t_{23} = 1.45, means ± SEM).

Supplementary Figure 6 - Dendritic spine density and spontaneous excitatory activity in 16p11.2$^{+/-}$ mutants.

(A) Quantification of dendritic spines in cortical layers 2/3 in the prefrontal cortex (PFC) and primary somatosensory (S1) cortical areas of 16p11.2$^{+/-}$ mice highlighted a significant reduction in dendritic spine density in the PFC, but not in S1, of 16p11.2 mutant mice compared to control littermates (***p<0.001, *t*-test). (B-E) Whole-cell patch clamp electrophysiological recordings in prefrontal pyramidal neurons of 16p11.2$^{+/-}$ mice did not reveal genotype-dependent differences in spontaneous and miniature excitatory post-synaptic currents. (B) Representative sEPSC recordings and averaged sEPSC

traces in PFC pyramidal neurons. (C) Amplitude (+/+: 6.58 ± 0.66 pA, +/-: 7.70 ± 0.87 pA) and frequency (+/+: 3.16 ± 0.80 Hz, +/-: 3.64 ± 0.65 Hz) of sEPSCs in +/+ (n=10) and +/- (n=9) neurons did not exhibit any significant inter-group differences. (D) Representative mEPSC recordings and averaged mEPSC traces in PFC pyramidal neurons. (E) Amplitude (+/+: 5.07 ± 0.29 pA, +/-: 5.84 ± 0.59 pA) and frequency (+/+: 1.71 ± 0.54 Hz, +/-: 2.61 ± 0.73 Hz) of mEPSCs in +/+ (n=10) and +/- (n=9) neurons did not exhibit any significant inter-group differences. Group data are shown as means ± SEM.

References

Anagnostou E, Taylor M. Review of neuroimaging in autism spectrum disorders: what have we learned and where we go from here. Molecular Autism 2011; 2(1): 4.

Balsters JH, Mantini D, Wenderoth N. Connectivity-based parcellation reveals distinct cortico-striatal connectivity fingerprints in Autism Spectrum Disorder. NeuroImage 2017.

Bernhardt BC, Valk SL, Silani G, Bird G, Frith U, Singer T. Selective Disruption of Sociocognitive Structural Brain Networks in Autism and Alexithymia. Cerebral Cortex 2014; 24(12): 3258-67.

Blakemore S-J. The social brain in adolescence. Nat Rev Neurosci 2008; 9(4): 267-77.

Blumenthal I, Ragavendran A, Erdin S, Klei L, Sugathan A, Guide Jolene R*, et al.* Transcriptional Consequences of 16p11.2 Deletion and Duplication in Mouse Cortex and Multiplex Autism Families. The American Journal of Human Genetics 2014; 94(6): 870-83.

Cardin JA, Carl+¬n M, Meletis K, Knoblich U, Zhang F, Deisseroth K*, et al.* Driving fast-spiking cells induces gamma rhythm and controls sensory responses. Nature 2009; 459(7247): 663-7.

Carlén M. What constitutes the prefrontal cortex? Science 2017; 358(6362): 478-82.

Chang YS, Owen JP, Pojman NJ, Thieu T, Bukshpun P, Wakahiro ML*, et al.* Reciprocal white matter alterations due to 16p11. 2 chromosomal deletions versus duplications. Human brain mapping 2016; 37(8): 2833-48.

Chen JA, Penaagarikano O, Belgard TG, Swarup V, Geschwind DH. The Emerging Picture of Autism Spectrum Disorder: Genetics and Pathology. Annual Review of Pathology: Mechanisms of Disease 2015; 10(1): 111-44.

Cheng W, Rolls ET, Gu H, Zhang J, Feng J. Autism: reduced connectivity between cortical areas involved in face expression, theory of mind, and the sense of self. Brain 2015a.

Cheng W, Rolls ET, Gu H, Zhang J, Feng J. Autism: reduced connectivity between cortical areas involved in face expression, theory of mind, and the sense of self. Brain 2015b; 138(5): 1382-93.

Cole MW, Anticevic A, Repovs G, Barch D. Variable Global Dysconnectivity and Individual Differences in Schizophrenia. Biological Psychiatry 2011; 70(1): 43-50.

Cole MW, Pathak S, Schneider W. Identifying the brain's most globally connected regions. NeuroImage 2010; 49(4): 3132-48.

Cole MW, Yarkoni T, Repovš G, Anticevic A, Braver TS. Global connectivity of prefrontal cortex predicts cognitive control and intelligence. Journal of Neuroscience 2012; 32(26): 8988-99.

Cunningham SI, Tomasi D, Volkow ND. Structural and functional connectivity of the precuneus and thalamus to the default mode network. Human Brain Mapping 2017; 38(2): 938-56.

de la Torre-Ubieta L, Won H, Stein JL, Geschwind DH. Advancing the understanding of autism disease mechanisms through genetics. Nat Med 2016; 22(4): 345-61.

Di Martino A, Yan CG, Li Q, Denio E, Castellanos FX, Alaerts K*, et al.* The autism brain imaging data exchange: towards a large-scale evaluation of the intrinsic brain architecture in autism. Mol Psychiatry 2013.

Dodero L, Damiano M, Galbusera A, Bifone A, Tsaftsaris SA, Scattoni ML*, et al.* Neuroimaging Evidence of Major Morpho-Anatomical and Functional Abnormalities in the BTBR T+TF/J Mouse Model of Autism. PLoS ONE 2013; 8(10): e76655.

Dosenbach NUF, Nardos B, Cohen AL, Fair DA, Power JD, Church JA*, et al.* Prediction of Individual Brain Maturity Using fMRI. Science 2010; 329(5997): 1358-61.

Falahpour M, Thompson WK, Abbott AE, Jahedi A, Mulvey ME, Datko M*, et al.* Underconnected, But Not Broken? Dynamic Functional Connectivity MRI Shows Underconnectivity in Autism Is Linked to Increased Intra-Individual Variability Across Time. Brain Connect 2016; 6(5): 403-14.

Ferrari L, Turrini G, Crestan V, Bertani S, Cristofori P, Bifone A*, et al.* A robust experimental protocol for pharmacological fMRI in rats and mice. Journal of Neuroscience Methods 2012; 204(1): 9-18.

Giorgi A, Migliarini S, Galbusera A, Maddaloni G, Mereu M, Margiani G*, et al.* Brainwide mapping of endogenous serotonergic transmission via chemogenetic-fMRI. Cell Reports 2017; In press.

Glausier JR, Lewis DA. Dendritic spine pathology in schizophrenia. Neuroscience 2013; 251: 90-107.

Golzio C, Willer J, Talkowski ME, Oh EC, Taniguchi Y, Jacquemont S*, et al.* KCTD13 is a major driver of mirrored neuroanatomical phenotypes of the 16p11.2 copy number variant. Nature 2012; 485(7398): 363-7.

Gozzi A, Schwarz AJ. Large-scale functional connectivity networks in the rodent brain. NeuroImage 2015.

Grossmann T. The role of medial prefrontal cortex in early social cognition. Frontiers in Human Neuroscience 2013; 7(340).

Hanson E, Bernier R, Porche K, Jackson FI, Goin-Kochel RP, Snyder LG*, et al.* The cognitive and behavioral phenotype of the 16p11. 2 deletion in a clinically ascertained population. Biological psychiatry 2015; 77(9): 785-93.

Hoover W, Vertes R. Anatomical analysis of afferent projections to the medial prefrontal cortex in the rat. Brain Struct Funct 2007; 212(2): 149-79.

Horev G, Ellegood J, Lerch JP, Son YEE, Muthuswamy L, Vogel H*, et al.* Dosage-dependent phenotypes in models of 16p11.2 lesions found in autism. Proceedings of the National Academy of Sciences of the United States of America 2011; 108(41): 17076-81.

Hull JV, Jacokes ZJ, Torgerson CM, Irimia A, Van Horn JD. Resting-State Functional Connectivity in Autism Spectrum Disorders: A Review. Frontiers in Psychiatry 2017; 7(205).

Kumar RA, KaraMohamed S, Sudi J, Conrad DF, Brune C, Badner JA*, et al.* Recurrent 16p11.2 microdeletions in autism. Human Molecular Genetics 2008; 17(4): 628-38.

Liska A, Bertero A, Gomolka R, Sabbioni M, Galbusera A, Barsotti N*, et al.* Homozygous loss of autism-risk gene CNTNAP2 results in reduced local and long-range prefrontal functional connectivity. Cereb Cortex 2017; 10: 1.

Liska A, Galbusera A, Schwarz AJ, Gozzi A. Functional connectivity hubs of the mouse brain. NeuroImage 2015; 115(0): 281-91.

Liu X, Zhu XH, Zhang Y, Chen W. Neural origin of spontaneous hemodynamic fluctuations in rats under burst-suppression anesthesia condition. Cereb Cortex 2011; 21(2): 374-84.

Lu H, Zuo Y, Gu H, Waltz JA, Zhan W, Scholl CA*, et al.* Synchronized delta oscillations correlate with the resting-state functional MRI signal. ProcNatlAcadSciUSA 2007; 104(46): 18265-9.

Maillard AM, Ruef A, Pizzagalli F, Migliavacca E, Hippolyte L, Adaszewski S*, et al.* The 16p11.2 locus modulates brain structures common to autism, schizophrenia and obesity. Mol Psychiatry 2015; 20(1): 140-7.

Malhotra D, Sebat J. CNVs: Harbingers of a Rare Variant Revolution in Psychiatric Genetics. Cell 2012; 148(6): 1223-41.

Marín O. Interneuron dysfunction in psychiatric disorders. Nat Rev Neurosci 2012; 13(2): 107-20.

Martino A, Ettorre M, Musilli M, Lorenzetto E, Buffelli M, Diana G. Rho GTPase-dependent plasticity of dendritic spines in the adult brain. Front Cell Neurosci 2013; 7: 62.

McCormick A, Pape H-C. Properties of a hyperpolarization□activated cation current and its role in rhythmic oscillation in thalamic relay neurones. The Journal of physiology 1990; 431(1): 291-318.

Michetti C, Caruso A, Pagani M, Sabbioni M, Medrihan L, David G*, et al.* The Knockout of Synapsin II in Mice Impairs Social Behavior and Functional Connectivity Generating an ASD-like Phenotype. Cerebral Cortex 2017; 27(10): 5014-23.

Osakada F, Callaway EM. Design and generation of recombinant rabies virus vectors. Nature protocols 2013; 8(8): 1583-601.

Owen JP, Chang YS, Pojman NJ, Bukshpun P, Wakahiro MLJ, Marco EJ*, et al.* Aberrant White Matter Microstructure in Children with 16p11.2 Deletions. The Journal of Neuroscience 2014; 34(18): 6214-23.

Pagani M, Liska A, Galbusera A, Gozzi A. Altered prefrontal functional connectivity and anatomy in mice lacking autism-associated gene Shank3. Society for Neuroscience Annual Meeting, 2017; 2017; Washington; 2017.

Paul LK, Corsello C, Kennedy DP, Adolphs R. Agenesis of the corpus callosum and autism: a comprehensive comparison. Brain 2014; 137(6): 1813-29.

Peters A. Examining neocortical circuits: some background and facts. J Neurocytol 2002; 31(3-5): 183-93.

Power JD, Barnes KA, Snyder AZ, Schlaggar BL, Petersen SE. Spurious but systematic correlations in functional connectivity MRI networks arise from subject motion. NeuroImage 2012; 59(3): 2142-54.

Power JD, Schlaggar BL, Petersen SE. Recent progress and outstanding issues in motion correction in resting state fMRI. NeuroImage 2015; 105(0): 536-51.

Pucilowska J, Vithayathil J, Tavares EJ, Kelly C, Karlo JC, Landreth GE. The 16p11.2 Deletion Mouse Model of Autism Exhibits Altered Cortical Progenitor Proliferation and Brain Cytoarchitecture Linked to the ERK MAPK Pathway. The Journal of Neuroscience 2015; 35(7): 3190-200.

Qureshi AY, Mueller S, Snyder AZ, Mukherjee P, Berman JI, Roberts TP. Opposing brain differences in 16p11.2 deletion and duplication carriers. J Neurosci 2014; 34.

Riccomagno MM, Kolodkin AL. Sculpting Neural Circuits by Axon and Dendrite Pruning. Annual Review of Cell and Developmental Biology 2015; 31: 779-805.

Ripley B. MASS: Support functions and datasets for Venables and Ripley's MASS. R package version 7.3-40. 2015.

Robinson S, Todd TP, Pasternak AR, Luikart BW, Skelton PD, Urban DJ*, et al.* Chemogenetic silencing of neurons in retrosplenial cortex disrupts sensory preconditioning. Journal of Neuroscience 2014; 34(33): 10982-8.

Rubinov M, Sporns O. Weight-conserving characterization of complex functional brain networks. NeuroImage 2011; 56(4): 2068-79.

Rudie J-á, Hernandez L-á, Brown J-á, Beck-Pancer D, Colich N-á, Gorrindo P*, et al.* Autism-Associated Promoter Variant in MET Impacts Functional and Structural Brain Networks. Neuron 2012; 75(5): 904-15.

Scott-Van Zeeland AA, Abrahams BS, Alvarez-Retuerto AI, Sonnenblick LI, Rudie JD, Ghahremani D*, et al.* Altered Functional Connectivity in Frontal Lobe Circuits Is Associated with Variation in the Autism Risk Gene CNTNAP2. Science Translational Medicine 2010; 2(56): 56ra80-56ra80.

Sforazzini F, Bertero A, Dodero L, David G, Galbusera A, Scattoni M*, et al.* Altered functional connectivity networks in acallosal and socially impaired BTBR mice. Brain Struct Funct 2014: 1-14.

Simons VIP Consortium. Simons Variation in Individuals Project (Simons VIP): a genetics-first approach to studying autism spectrum and related neurodevelopmental disorders. Neuron 2012; 73(6): 1063-7.

Sowell ER, Thompson PM, Holmes CJ, Jernigan TL, Toga AW. In vivo evidence for post-adolescent brain maturation in frontal and striatal regions. Nature neuroscience 1999; 2(10): 859-61.

Steffey MA, Brosnan RJ, Steffey EP. Assessment of halothane and sevoflurane anesthesia in spontaneously breathing rats. American Journal of Veterinary Research 2003; 64(4): 470-4.

Suetterlin P, Hurley S, Mohan C, Riegman KLH, Pagani M, Caruso A*, et al.* Early postnatal brain overgrowth and gene expression changes prefigure functional over-connectivity of the cortex in Chd8 haploinsufficient mice. bioRxiv 2017.

Supekar K, Uddin L-á, Khouzam A, Phillips J, Gaillard W-á, Kenworthy L-á*, et al.* Brain Hyperconnectivity in Children with Autism and its Links to Social Deficits. Cell Reports 2013; 5(3): 738-47.

Thompson AD, Picard N, Min L, Fagiolini M, Chen C. Cortical Feedback Regulates Feedforward Retinogeniculate Refinement. Neuron 2016; 91(5): 1021-33.

Tick B, Bolton P, Happé F, Rutter M, Rijsdijk F. Heritability of autism spectrum disorders: a meta-analysis of twin studies. Journal of Child Psychology and Psychiatry 2016; 57(5): 585-95.

Tyszka JM, Kennedy DP, Adolphs R, Paul LK. Intact Bilateral Resting-State Networks in the Absence of the Corpus Callosum. The Journal of Neuroscience 2011; 31(42): 15154-62.

Vasa RA, Mostofsky SH, Ewen JB. The disrupted connectivity hypothesis of autism spectrum disorders: Time for the next phase in research. Biological Psychiatry: Cognitive Neuroscience and Neuroimaging 2016.

Vogt B, Paxinos G. Cytoarchitecture of mouse and rat cingulate cortex with human homologies. Brain Struct Funct 2014; 219(1): 185-92.

Washington SD, Gordon EM, Brar J, Warburton S, Sawyer AT, Wolfe A*, et al.* Dysmaturation of the default mode network in autism. Human brain mapping 2014; 35(4): 1284-96.

Whitlock JR. Posterior parietal cortex. Current Biology 2017; 27(14): R691-R5.

Zhan Y, Paolicelli R, Sforazzini F, Weinhard L, Bolasco G, Pagani F*, et al.* Deficient neuron-microglia signaling results in impaired functional brain connectivity and social behavior. NatNeurosci 2014; 17: 400-6.

Zufferey F, Sherr EH, Beckmann ND, Hanson E, Maillard AM, Hippolyte L*, et al.* A 600 kb deletion syndrome at 16p11.2 leads to energy imbalance and neuropsychiatric disorders. Journal of Medical Genetics 2012; 49(10): 660-8.

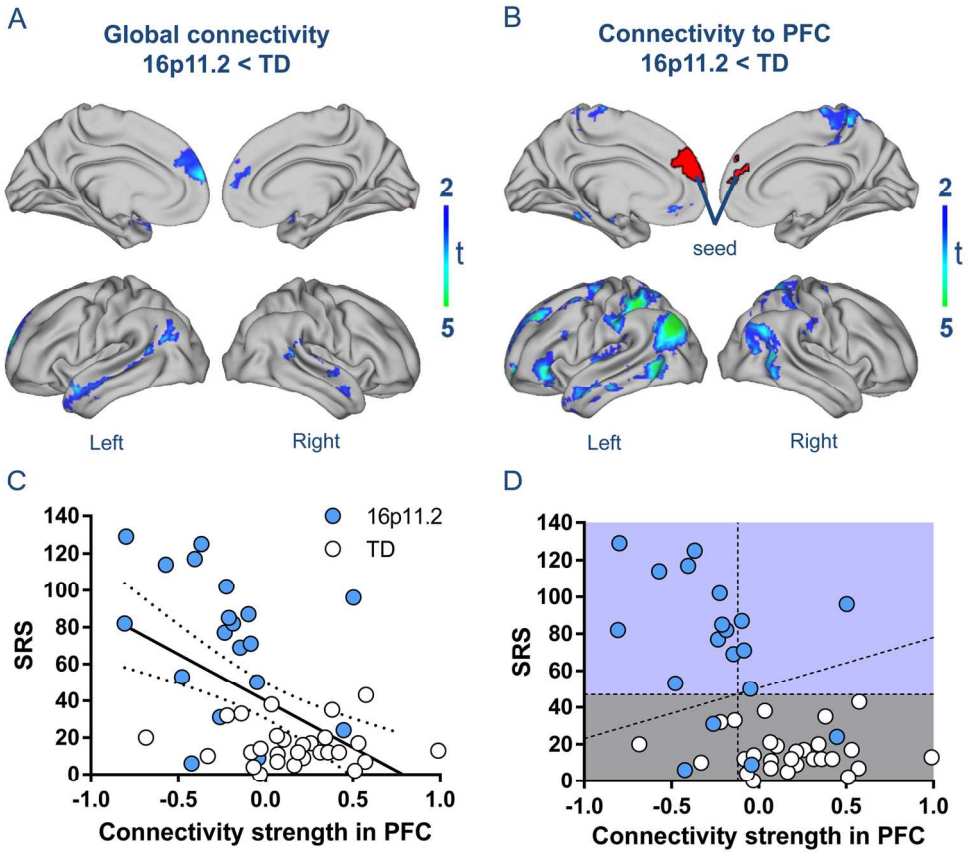

Figure 1 - Reduced prefrontal connectivity in 16p11.2 deletion carriers.
(A) Whole-brain voxel-wise mapping of intergroup differences in rsfMRI connectivity revealed reduced global connectivity in the medial prefrontal cortex (PFC) of 16p11.2 deletion carriers ($p < 0.05$, cluster-corrected) with respect to typically developing (TD) control subjects. Additional foci of reduced connectivity were located in temporal and parietal areas (superior and medial temporal gyrus, and temporal-parietal junctions). (B) Targets of the PFC underconnectivity, identified using a seed-based analysis. We used a seed region (shown in red) covering the whole PFC area exhibiting significant inter-group differences in Figure 1A. Functional connectivity reductions were observed in the latero-temporal cortex, and inferior parietal lobule, as well as in the superior and inferior frontal cortex and paracentral gyrus of 16p11.2 deletion carriers ($p < 0.05$, cluster corrected). (C) PFC connectivity strength exhibited robust inverse correlation with SRS score ($r = -0.52$, $p < 0.001$). (D) Linear discrimination analysis of the predictive power of PFC connectivity and SRS score of CNV in individual subjects. SRS score and connectivity strength were assessed either alone (vertical and horizontal dashed line, respectively) or in combination (diagonal dashed line).

163x144mm (300 x 300 DPI)

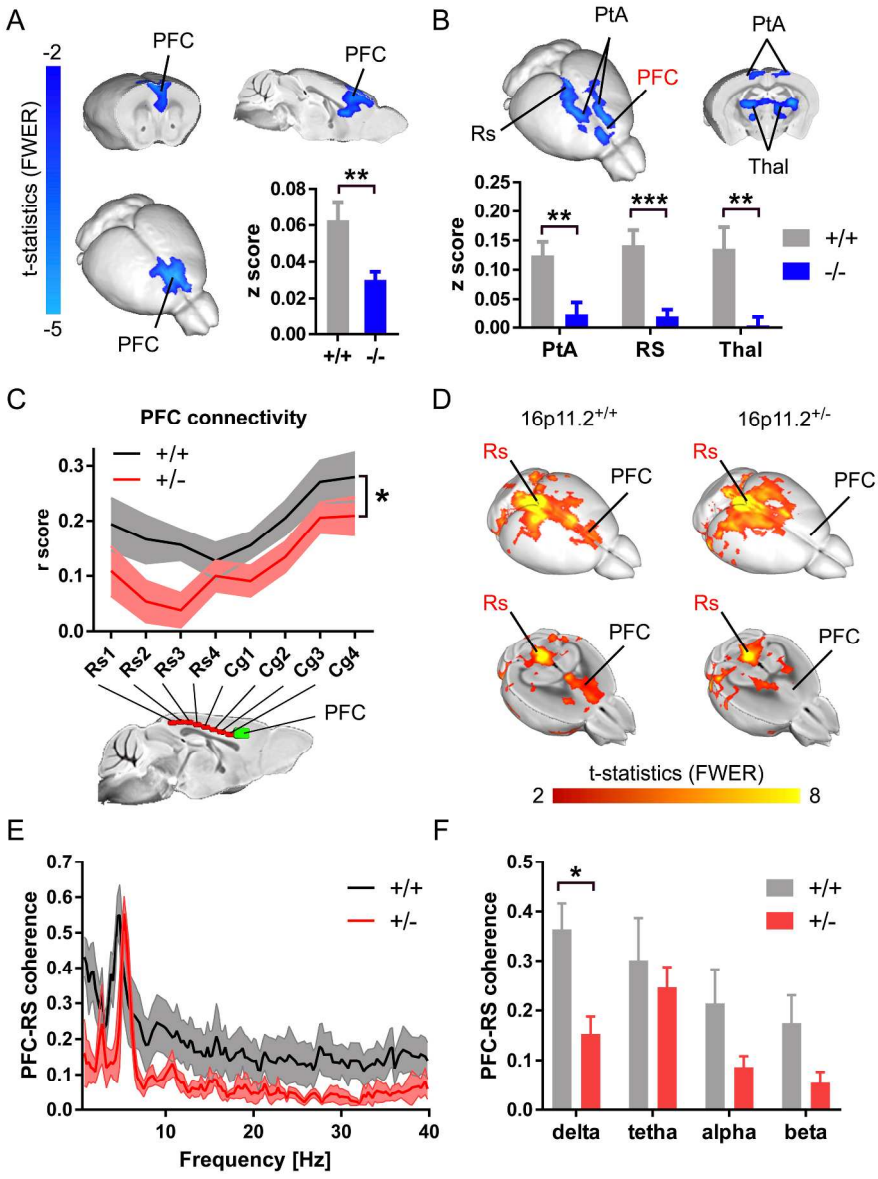

Figure 2 - Reduced prefrontal connectivity and low-frequency synchronization in 16p11.2+/- mice. (A) Whole-brain voxel-wise mapping of global connectivity revealed reduced functional connectivity in the medial prefrontal cortex (PFC) of 16p11.2+/- mutant mice compared to control littermates ($p < 0.05$, cluster-corrected). (B) Seed-based mapping of the prefrontal cortex (green seed, Figure 2C) revealed foci of reduced rsfMRI connectivity in parieto-temporal areas (PtA), retrosplenial cortex (Rs) and thalamus (Thal) of 16p11.2+/- mutants ($p < 0.05$, cluster-corrected). Inset plots show a quantification of the effect size in the regions affected (*$p < 0.05$, **$p < 0.01$, ***$p < 0.001$, student t test, means ± SEM) (C) Connectivity profile between a series of midline seeds (Cg : cingulate cortex) and the prefrontal cortex (PFC, green) (*$p < 0.05$, two-way repeated measures ANOVA, mean ± SEM). (D) Seed correlation maps in control and 16p11.2 mutants highlighting reduced extension of long-range connectivity between the retrosplenial and prefrontal cortices (seed Rs3, $p < 0.05$ FWE cluster-corrected). (E, F) Local field potential (LFP) coherence measurements highlighted a reduction in long-range LFP coherence in 16p11.2+/- mice, resulting in a robust genotype x frequency interaction ($F_{191,1910} = 2.487$, $p < 0.001$, Figure 2E, means ± SEM) and a

significant reduction in delta frequency range (*p < 0.05, Figure 2F, means ± SEM).

247x332mm (300 x 300 DPI)

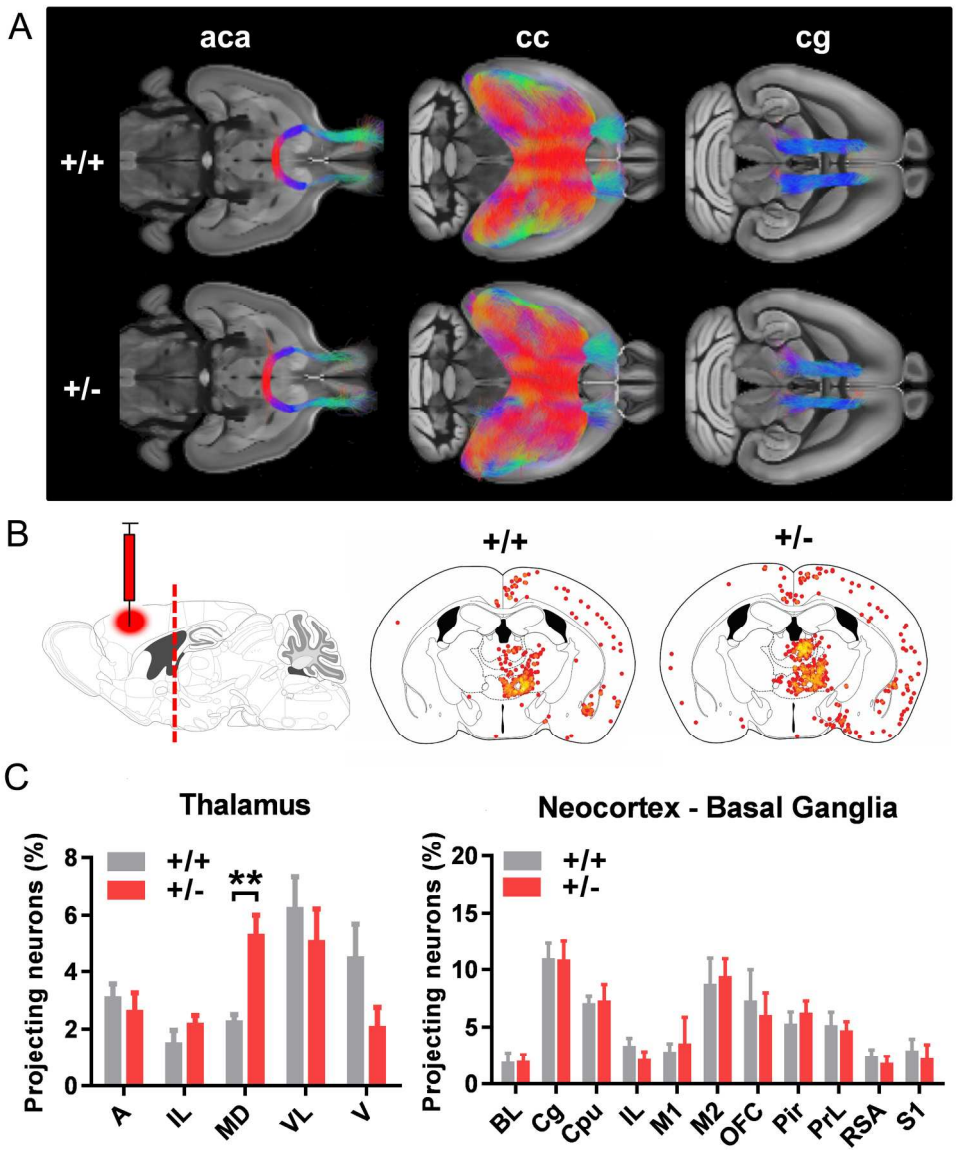

Figure 3 - Altered thalamo-frontal wiring in 16p11.2+/- mice.
(A) Anterior commissure, corpus callosum and cingulum tracts virtually dissected in two representative mice (16p11.2+/+ top, 16p11.2+/− bottom). We did not observe any genotype-dependent differences in the macroscale organization of these major white matter tracts (Supplementary Figure S5). (B) Regional distribution of retrogradely labelled cells in the thalamus of control (16p11.2+/+) and 16p11.2+/− mutant mice after injection of recombinant rabies virus in the prefrontal cortex. (C) Quantification of the frequency of retrogradely labelled cells in neocortical areas and sub-thalamic regions revealed focally increased projection frequency in the mediodorsal thalamus (MD) of 16p11.2+/− mice (**p< 0.01, FDR corrected, means ± SEM). A: anterior thalamus, MD: mediodorsal thalamus, IL: intralaminar thalamus, V: ventral thalamus, VL: ventrolateral thalamus, BL: basolateral amygdala, Cg: cingulate cortex, Cpu: caudate putamen, IL: infralimbic cortex, M1: primary motor cortex, M2: secondary motor cortex, OFC: orbitofrontal cortex, Pir: piriform cortex, PrL: prelimbic cortex, RSA: retrosplenial cortex, S1: somatosensory cortex.

217x256mm (300 x 300 DPI)

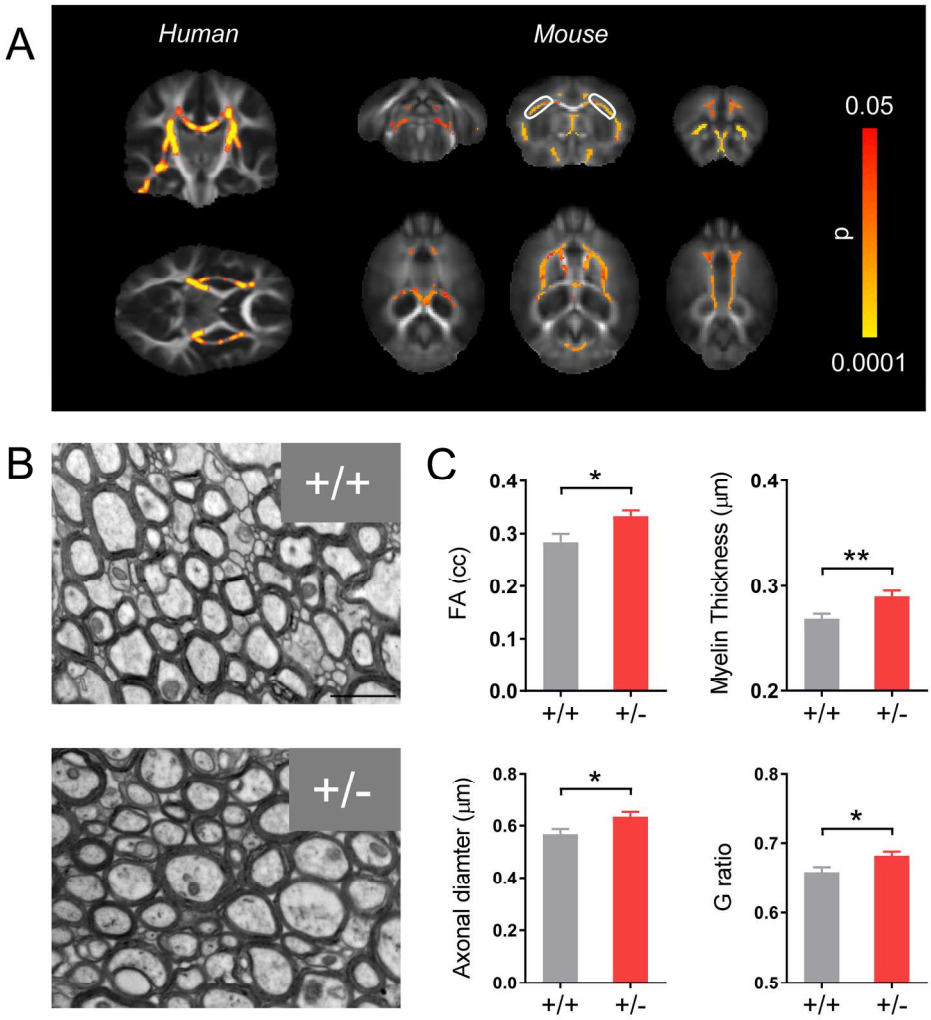

Figure 4 – Comparable white matter microstructural abnormalities in human 16p11.2 deletion carriers and 16p11.2+/- mice.
(A) White matter regions exhibiting significantly increased fractional anisotropy (FA) in human deletion carriers (left, modified from Owen et al. 2014, with permission). Voxelwise mapping of FA in mouse revealed analogous increases in 16p11.2+/- mutants (right). (B) Transmission electron micrographs of corpus callosum cross-sections from control (+/+) and 16p11.2+/- (+/-) mice. Scale bar, 1 µm; original magnification ×25K. (C) Quantification of fractional anisotropy, mean thickness, axonal diameter and G ratio in callosal neurons (*p <0.05, **p < 0.01, means ± SEM).

204x226mm (300 x 300 DPI)

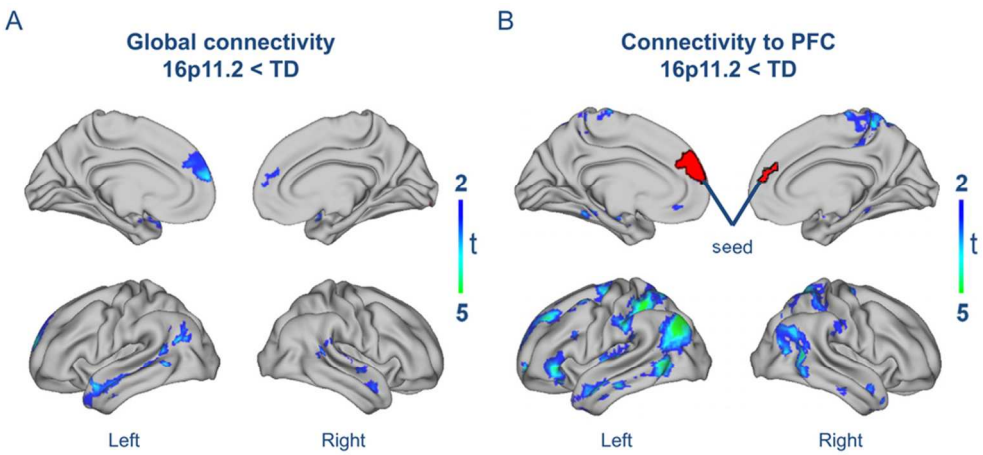

85x38mm (300 x 300 DPI)

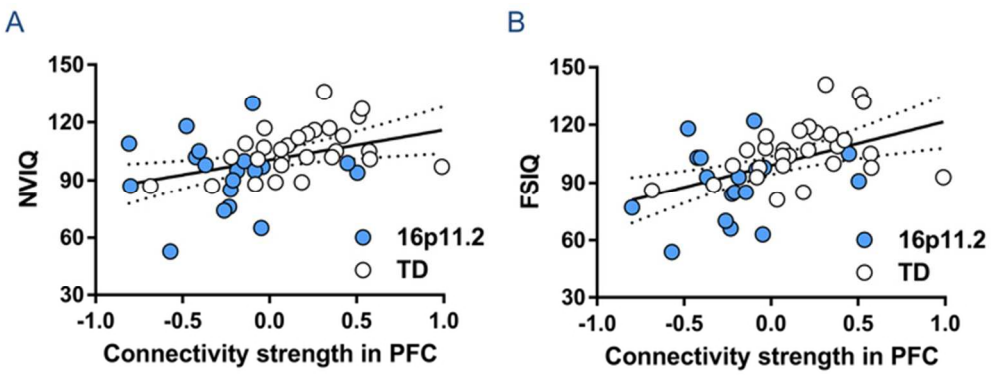

64x24mm (300 x 300 DPI)

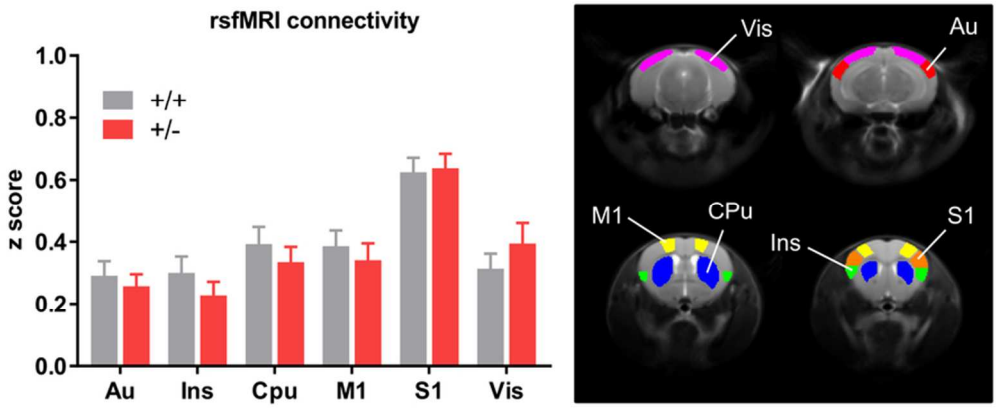

75x31mm (300 x 300 DPI)

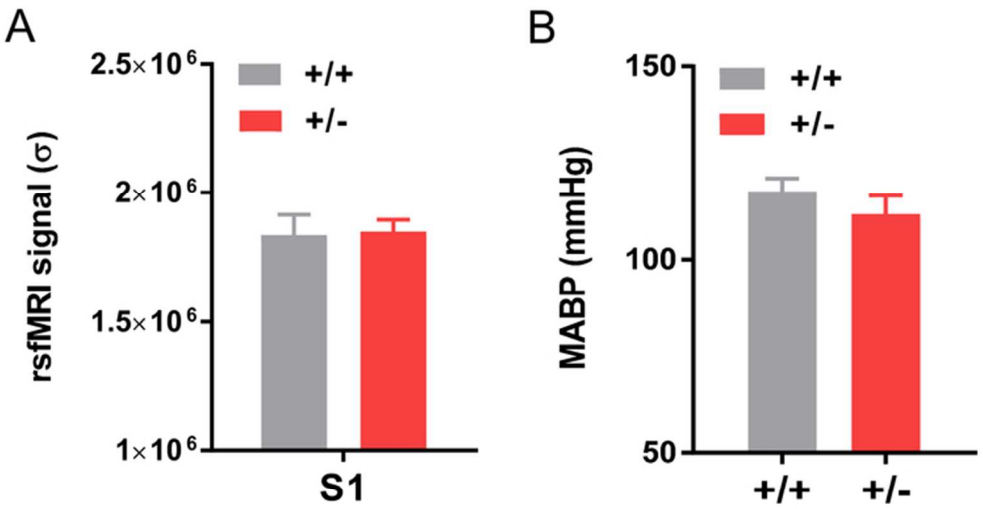

64x38mm (300 x 300 DPI)

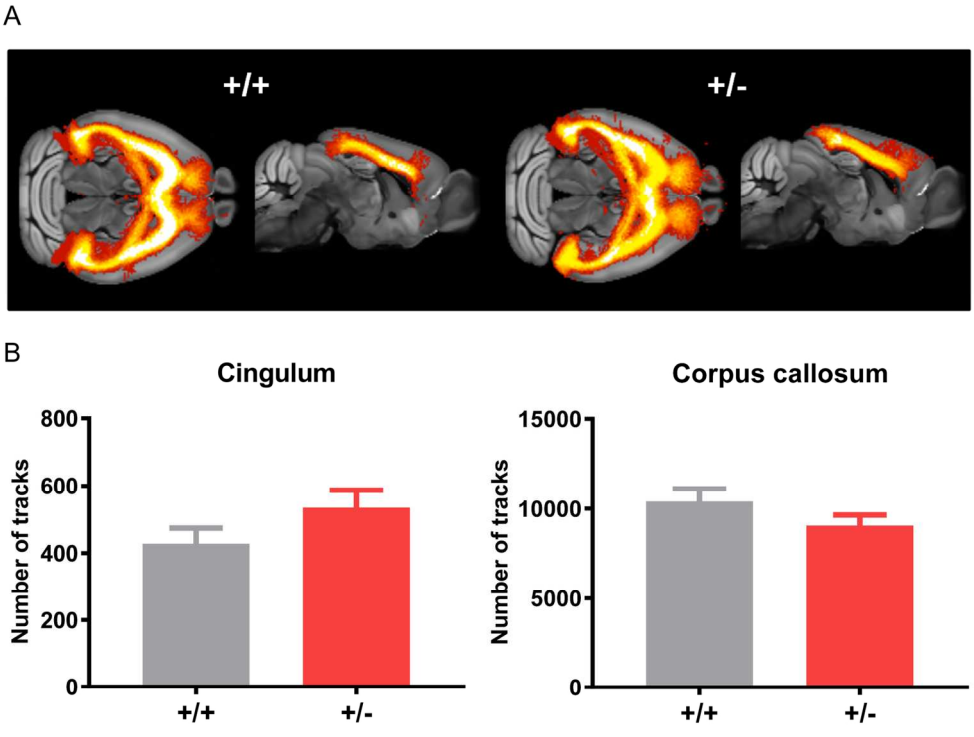

146x115mm (300 x 300 DPI)

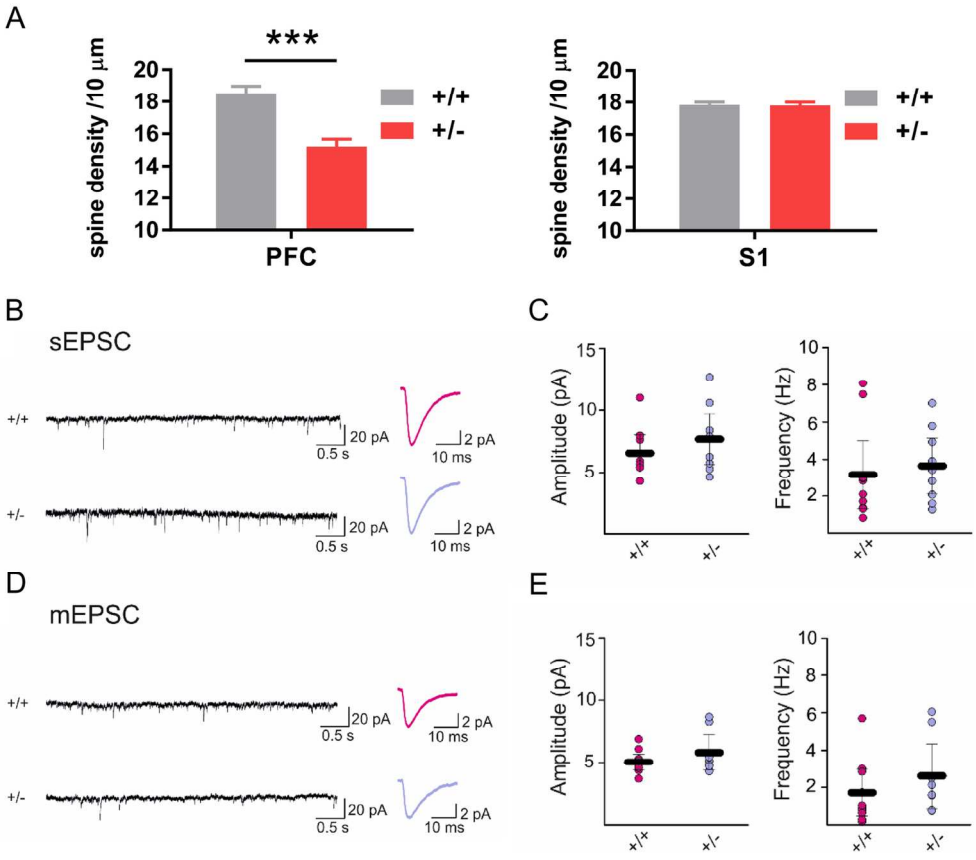

142x122mm (300 x 300 DPI)

Table I: Demographics

	Pediatric controls	Pediatric 16p11.2 del carriers
Age (years)	12.49±2.24	11.52±2.53
Gender	16M/12F	10M/9F
NVIQ**	105±12	93±18
FSIQ**	106±15	89±18
SRS***	16±11	74±37

**p<0.01, ***p<0.001, *t*-test

Table SI. Diagnoses in the deletion carriers

Diagnosis	Pediatric deletion carriers (n=19)
ADHS	7
Anxiety	3
Articulation disorder	12
Behavioral disorder	1
ASD	7
Coordination disorder	5
Enuresis disorder	3
Language disorder	8
Learning disorder	2
Mood disorder	0
Intellectual disability	2
Stereotyped motor disorder	0
Tic/Tourette's	2

Each carrier may have more than one diagnosis.
ADHS: attention-deficit hyperactivity syndrome; ASD: autism spectrum disorder

Table SII: Full subject list after exclusion for motion parameters

subject	group	gender	age	NVIQ	FSIQ	site	Scans available	Scrubbed volumes	FD
14817-x1	controls	female	130	105	105	60	2	0.03	0.1366
14837-x1	controls	male	164	116	116	60	1	0	0.0685
14847-x1	controls	female	180	107	108	60	1	0.07	0.1336
14851-x1	controls	female	108	87	89	60	1	0.03	0.1249
14855-x1	controls	female	181	97	93	50	1	0.04	0.1216
14856-x1	controls	male	176	101	98	60	2	0.07	0.1374
14861-x1	controls	female	113	101	107	50	1	0.02	0.0845
14865-x1	controls	female	141	88	93	50	2	0.18	0.1573
14871-x1	controls	female	165	123	136	60	1	0	0.0683
14897-x1	controls	male	165	109	107	60	1	0	0.0823
14915-x2	controls	male	88	105	109	60	1	0.10	0.1891
14923-x1	controls	male	184	117	114	60	1	0	0.0758
14927-x2	controls	female	119	89	81	50	1	0.19	0.2516
14930-x1	controls	male	125	108	104	50	1	0.08	0.1735
14931-x1	controls	male	160	136	141	60	1	0.03	0.1010
14935-x2	controls	female	170	106	104	50	1	0	0.0758
14944-x1	controls	male	150	87	86	50	1	0	0.0759
14948-x1	controls	male	135	102	107	60	1	0.08	0.1019
14960-x1	controls	male	130	102	99	60	1	0.03	0.1069
14961-x1	controls	male	125	127	132	60	1	0.03	0.1024
14972-x1	controls	female	126	114	119	60	1	0.19	0.1854
14979-x1	controls	male	184	98	99	50	2	0.19	0.2063
14979-x2	controls	female	147	102	100	50	1	0.19	0.1978
14983-x1	controls	male	180	117	115	60	2	0	0.0828
14985-x1	controls	male	186	112	117	60	1	0.19	0.1570
15043-x1	controls	female	142	113	112	60	2	0.03	0.1912
15048-x1	controls	male	151	101	98	50	1	0	0.0795
15090-x1	controls	male	170	89	85	50	1	0	0.0763
14729-x5	deletions	male	99	76	66	60	1	0.16	0.1601
14732-x6	deletions	female	131	53	54	60	1	0.07	0.1531
14744-x5	deletions	male	186	94	91	50	1	0	0.0913
14748-x1	deletions	female	120	74	70	50	1	0.13	0.1822
14761-x13	deletions	female	123	97	98	60	2	0	0.1347
14761-x14	deletions	male	145	102	103	60	2	0.19	0.2553
14786-x24	deletions	male	147	65	63	60	1	0.19	0.1968
14791-x26	deletions	female	85	95	93	60	1	0.12	0.1566
14792-x10	deletions	male	93	99	105	50	1	0.04	0.1030
14799-x1	deletions	male	174	130	122	50	1	0	0.1790
14824-x12	deletions	male	172	105	103	60	1	0	0.1347
14824-x13	deletions	male	172	98	93	60	2	0.03	0.1834
14858-x3	deletions	female	151	85	84	50	2	0.08	0.1069
14869-x13	deletions	female	179	118	118	50	1	0	0.0920
14895-x3	deletions	female	132	90	85	50	1	0.04	0.1582

14924-x1	deletions	female	101	109		60	1	0	0.0748
14970-x7	deletions	female	124	100	85	50	2	0.04	0.1582
14971-x9	deletions	male	144	87	77	60	1	0.05	0.1688
15083-x5	deletions	male	149	95	97	50	1	0	0.1350

Supplemental Experimental Methods

Human rsfMRI

Ethical Statement

All study procedures were approved by the institutional review board at the involved medical centers and are in accordance with the ethical standards of the Helsinki Declaration of 1975, as revised in 2008.

Resting-State fMRI

All MR imaging was performed on 3T Tim Trio MR scanners (Siemens) one each of two sites, UC Berkeley or at the Children's Hospital of Philadelphia (CHOP), using 32-channel phased-array radiofrequency head coils. High-resolution structural MR imaging of the brain was performed with an axial 3D magnetization-prepared rapid acquisition gradient-echo (MPRAGE) T1-weighted sequence (TE=1.64 ms; TR=2530 ms; TI=1200 ms; flip angle=7°) with a 256 mm field of view, and 160 1.0 mm contiguous partitions at a 256 x 256 matrix. rsfMRI timeseries were acquired using the following imaging parameters: acquisition matrix, 72 x 72 x 47, FOV, 216 x 216 mm^2, slice thickness 3 mm, TR = 3000 ms, TE = 30 ms, α = 90°, number of repetitions = 124 for a total scan time of 6'12''.

Sample selection and image preprocessing

A detailed description of subject recruitment and diagnostic criteria has been recently provided by Chang et al., (2016). Imaging analyses focused on initially identified probands and their siblings with deletion at 16p11.2 as part of a multi-center investigation of 16p11.2 deletion carriers (Simons VIP Consortium, 2012). We removed one deletion

subject whose age was 2 standard deviations above the mean of the patient group (130 ± 35 months). All control subjects whose age was within 2 standard deviations of the mean age of the remaining group of patients (127 ± 30 months) were selected for further analyses. This resulted in an initial set of scans encompassing 38 patients and 40 controls. After strict control for motion (described below) we excluded 19 patients and 12 control subjects, resulting in a final list of 19 and pediatric deletion carriers (age 8–16 years; 10 males and 9 females) and 28 pediatric controls (age 7–16 years; 16 males and 12 females). A breakdown of subject demographics is given in Table I, while Supplementary Table 2 reports patient code and corresponding demographics for each of the subjects analyzed in this study. All children were administered the Differential Ability Scales-Early Years & School Age (DASII) Intelligence Test for Children (WISC), from which full-scale IQ (FSIQ) and NVIQ sub-scores were used for further analysis. The children did also undergo testing for socio-cognitive abilities using social responsiveness scale (SRS).

Image preprocessing was based on previous studies of the ABIDE dataset (Di Martino *et al.*, 2013) and on the Preprocessed Connectomes Project (http://preprocessed-connectomes-project.org/abide/cpac.html). In brief, the structural images were skull-stripped (AFNI/3dSkullStirp), segmented (FSL/FAST) and normalized to MNI152 (ANTs). Functional images were slice time corrected (AFNI/3dTshift), motion corrected (AFNI/3dvolreg) and skull striped (AFNI/3dAutomask). Nuisance signals including motion parameters (6 head motion parameters, 6 head motion parameters one time point before, 12 corresponding squared units), the top 5 principal components from the signal in the white-matter and cerebro-spinal fluid (Behzadi *et al.*, 2007) and linear and quadratic trends were regressed. The images were bandpass filtered (0.01 – 0.1 Hz) and registered to the anatomical space with a linear transformation (FSL/FLIRT) followed by a

white-matter boundary based transformation (FSL/FAST, FSL/FLIRT). To control for motion artefacts, we employed a scrubbing procedure and removed all frames whose framewise displacement (FD) was larger than 0.5mm (Power *et al.*, 2012; Di Martino *et al.*, 2013). Given the short extension of rsfMRI scans (124 frames), to increase confidence in our results we only retained subjects in which > 80% of rsfMRI volumes were retained after scrubbing. As most subjects underwent two resting-state acquisitions, we retained for each subject the acquisition with lowest motion as assessed with FD. We have reported the number of scrubbed volumes and mean FD for each subject in Supplementary Table 2. The fraction of scrubbed volumes was identical in both groups (6% ± 0.01, both groups). Mean FD was slightly higher in del vs. control children (0.15±0.01 and 0.13±0.01, respectively, p = 0.13, t_{45}= 1.54, *t*-test). The whole pre-processing pipeline was implemented using the Configurable Pipeline for the Analysis of Connectomes (C-PAC v1.0.1a, https://fcp-indi.github.io/). The configuration file we used is available upon request to the corresponding author.

Network centrality analyses

To obtain an unbiased mapping of inter-group connectivity differences, we calculated individual network centrality maps following Di Martino et al., (2013) as implemented in C-PAC. Specifically, for each voxel we calculated the sum of the weights (correlations) of all significant connections (p < 0.001) to all other voxels within a 25% grey-matter probability mask. Centrality indices were then transformed to z-scores based on each individual mean and standard deviation for centrality across all voxels. The maps were then smoothed (Gaussian filter with full width at half-maximum of 6mm) and normalized to MNI space. Intergroup differences were identified using two-sample t-tests (P < 0.05, family-wise error cluster-corrected, with cluster-defining threshold of t_{40} > 2.01, P < 0.05 as implemented in FSL) with age, gender, group-centered NVIQ, site and mean FD as

covariates. We subsequently performed seed analyses, using as seed the whole medial prefrontal area in which the deletion group showed significantly-reduced centrality. To identify group-differences in seed connectivity maps, we performed a two-sample t-test ($P < 0.05$ FWE cluster-corrected, with cluster-defining threshold of $t_{40} > 2.01$, $P < 0.05$ as implemented in FSL) with age, gender, group-centered NVIQ, site and mean FD as covariates.

Linear Discriminant Analysis (LDA) was performed on 16p11.2 del carriers and control subjects based on prefrontal global connectivity and SRS scores combined, or alone. Results were computed as sensitivity (percentage of 16p11.2 del carriers correctly classified as carriers), specificity (percentage of controls correctly classified as controls) and accuracy, the percentage of all subjects correctly classified. All analyses were performed using leave-one-out validation to avoid over-training of classifiers (Lerch *et al.*, 2008). LDA was performed using the MASS libraries v7.3 (Ripley, 2015) available in the R project (http://www.r-project.org).

Mouse Studies

Ethical Statement

All *in-vivo* animal studies were conducted in accordance with the Italian Law (DL 26/214, EU 63/2010, Ministero della Sanità, Roma) and the recommendations in the Guide for the Care and Use of Laboratory Animals of the National Institutes of Health. Animal research protocols were also reviewed and consented to by the animal care committee of the Istituto Italiano di Tecnologia. All surgical procedures were performed under anesthesia.

Functional and structural MRI

Animals

16p11.2$^{+/-}$ and control "wild-type" *16p11.2*$^{+/+}$ breeding pairs were obtained from Jackson Laboratories (Bar Harbor, ME, USA) and bred locally. Mice were housed by sex in mixed genotype groups, with temperature maintained at 21±1°C and humidity at 60±10%. All experiments were performed on adult male mice between 12-16 week of age, corresponding to young maturity.

Resting-State fMRI

rsfMRI experiments were performed on mice carrying 16p11.2 deletions and wild-type controls (n = 12 and n = 11, respectively). At the time of imaging, mice were 18-20 weeks old. The animal preparation protocol was recently described in greater detail (Ferrari *et al.*, 2012; Sforazzini *et al.*, 2014a). Briefly, mice were anaesthetized with isoflurane (5% induction), intubated and artificially ventilated (2% maintenance). The left femoral artery was cannulated for continuous blood pressure monitoring and terminal arterial blood sampling. At the end of surgery, isoflurane was discontinued and substituted with halothane (0.75%). Functional data acquisition commenced 45 min after isoflurane cessation. Mean arterial blood pressure was recorded throughout imaging sessions. Arterial blood gases (p_aCO_2 and p_aO_2) were measured at the end of the functional time series to exclude non-physiological conditions. Mean p_aCO_2 and p_aO_2 levels recorded were 21 ± 6 and 209 ± 66 mmHg in *16p11.2*$^{+/+}$ and 15 ± 6 and 200 ± 67 mmHg in *16p11.2*$^{+/-}$. Possible genotype-dependent differences in anesthesia sensitivity were evaluated using Student's two-sample *t*-test applied to two independent readouts previously shown to be linearly correlated with anesthesia depth: mean arterial blood pressure and amplitude of cortical BOLD signal fluctuations (Steffey *et al.*, 2003; Liu *et al.*, 2011; Zhan *et al.*, 2014).

rsfMRI images were acquired with a 7.0 Tesla MRI scanner (Bruker Biospin, Milan) as previously described (Liska *et al.*, 2015), using a 72 mm birdcage transmit coil and a four-channel solenoid coil for signal reception. For each session, high-resolution anatomical images were acquired with a fast spin echo sequence (repetition time (TR)/echo time (TE) 5500/60 ms, matrix 192 × 192, field of view 2 × 2 cm^2, 24 coronal slices, slice thickness 0.50 mm). Co-centered single-shot BOLD rsfMRI time series were acquired using an echo planar imaging sequence with the following parameters: TR/TE 1200/15 ms, flip angle 30°, matrix 100 × 100, field of view 2 × 2 cm^2, 24 coronal slices, slice thickness 0.50 mm, 500 volumes and a total rsfMRI acquisition time of 10 min. Readers can contact the corresponding author for access to the MRI raw data, templates and code employed to generate the functional maps.

Functional Connectivity Analyses

The first 20 volumes of the rsfMRI data were removed to allow for T1 equilibration effects. The time series were then despiked, corrected for motion and spatially normalized to an in-house mouse brain template (Sforazzini *et al.*, 2014b). The normalized data had a spatial resolution of 0.1042 × 0.1042 × 0.5 mm^3 (192 × 192 × 24 matrix). Head motion traces and mean ventricular signal (averaged rsfMRI time course within the subject's ventricular mask) were regressed out of each of the time series. No inter-group differences in ventricular volume was observed across groups as assessed by measuring the volumetric extension of individual ventricular masks (*t*-test, t_{21}=1.11, p=0.28). All rsfMRI time series were band-pass filtered to a frequency window of 0.01-0.1 Hz and spatially smoothed (full width at half maximum of 0.6 mm).

To obtain a spatially-unbiased mapping of inter-group differences in functional connectivity, we first mapped global connectivity strength in 16p11.2 mouse mutants and control littermates. This strategy entails a voxel-wise computation of the sum of the

weights (correlations) of all significant connections within a cerebral mask, and it is computationally equivalent to weighted network centrality mapped in humans (Liska *et al.*, 2015; Liska *et al.*, 2017). We next probed long-range functional connectivity using seed-based mapping and seed-to-VOI correlations. Seed placement is reported in Figure 2C. The chosen PFC seed is centered in the brain region exhibiting reduced global connectivity in 16p11.2 mutants (Fig. 1A), and straddles the prelimbic cortex and anterior cingulate cortex, two areas involved in class-common socio-cognitive functions that in primates are processed in the dorsomedial PFC and anterior-cingulate (reviewed by Carlén, 2017). Inter-group differences were assessed using a two-way repeated-measures ANOVA, where seed location and genotype were used as repeated-measure and between-group factor, respectively. Alterations in inter-hemispheric functional connectivity were assessed by computing correlation coefficients of inter-hemispheric volumes of interests (VOIs) depicted in Fig. S3. The statistical significance of inter-group correlation strength in each VOI was assessed with a two-tailed Student's *t*-test ($t > 2$, $p < 0.05$) and corrected for multiple comparisons using a false discovery rate $q = 0.05$ according to the Benjamini-Hochberg procedure.

Diffusion MRI

Ex vivo diffusion-weighted (DW) MRI was carried out on the same subjects employed for rsfMRI mapping in paraformaldehyde fixed specimens as previously described (Dodero *et al.*, 2013). The final set of experimental subjects included N=12 mutants, and N = 13 control subjects. The control group includes two additional control experimental subjects that we did not include in rsfMRI mapping owing to non-physiological parameters (blood pressure) and sever ghosting in rsfMRI images, respectively. At the end of the rsfMRI experiments, mice were transcardially perfused with 4% para-formaldehyde under deep isoflurane anesthesia. The perfusion solution was added with a Gadolinium chelate

(Prohance, Bracco, Milan) to reduce longitudinal relaxation times (Dodero *et al.*, 2013). Brains were imaged inside intact skulls to avoid post-extraction deformations. Each DW dataset was composed of 8 non-diffusion-weighted images and 81 different diffusion gradient-encoding directions with b=3000 s/mm2 (∂=6 ms, Δ=13 ms) acquired using an EPI sequence with the following parameters: TR/TE=13500/27.6 ms, field of view 1.68 × 1.54 cm^2, matrix 120 × 110, in-plane spatial resolution 140 x 140 μm^2, 54 coronal slices, slice thickness 280 µm, number of averages 20.

White Matter Fiber Tractography and Tract-Based Spatial Statistics

The DW datasets were first corrected for eddy current distortions (FSL/eddy_correct) and skull-stripped (Oguz *et al.*, 2014). The resulting individual brain masks were manually corrected using ITK-SNAP (Yushkevich *et al.*, 2006). Whole brain tractography was performed using MRtrix3 (Tournier *et al.*, 2012) using constrained spherical deconvolution (lmax = 8, (Tournier *et al.*, 2007)) and probabilistic tracking (iFOD2) with a FOD amplitude cut-off of 0.2. For each dataset, the whole brain mask was used as a seed, and a total of 100,000 streamlines were generated.

The corpus callosum and cingulum were selected as tracts of interest, given their major cortico-cortical extension and direct involvement in prefrontal-posterior connectivity (Vogt and Paxinos, 2014). The tracts were virtually dissected using TrackVis (http://www.trackvis.org/). Inter-group differences in streamline counts of the tracts were evaluated using a two-tailed Student's *t*-test ($t_{23} > 2.07$, $p < 0.05$). To provide a visual assessment of fiber distribution across groups, voxelwise parametric fiber density maps were generated using DiPy (Garyfallidis *et al.*, 2014), by determining for each voxel the number of subjects in which at least one streamline of the fiber tract of interest passes through the voxel. For visualization purposes, both the dissected tracts and group fiber

density maps were transformed to the Allen Mouse Common Coordinate Framework, Version 3 (http://www.brain-map.org/).

To enable a qualitative cross-comparison between white matter microstructural parameters in humans and mice, we mapped fractional anisotropy (FA) using Tract-Based Spatial Statistics (TBSS) analysis, as implemented in FSL (Dodero *et al.*, 2013). FA maps from all subjects were nonlinearly registered to an in-house FA template (FSL/FLIRT, FSL/FNIRT) and thinned using an FA threshold of 0.2 to create a skeleton of the white matter. Inter-group differences between deletion and control mice were evaluated with permutation testing using 5000 permutations ($p < 0.05$) using signal-to-noise ratio in diffusion weighted images as covariate of no interest to account for possible confounding contribution of the fixation procedure (Farrell *et al.*, 2007). No inter-group difference in the T1 relaxation time was observed, suggesting a comparable exposure to the gadolinium containing fixative in both groups (*t*-test, $t_{23} = 1.005$, $p = 0.33$).

In-vivo Electrophysiology

Experiments were performed on n = 6 control (16p11.2$^{+/+}$) and n = 6 mutant (16p11.2$^{+/-}$) littermates. At the time of the surgery the mice were from 11 to 13 weeks old, with a mean body weight of 25.3± 1.1 grams. After surgery mice were singly-housed until the end of the tests.

Electrodes implantation was performed under deep anesthesia (isoflurane 4%). The skull surface was exposed and two stainless steel screws were fixed permanently into the posterior and anterior portions of the skull, to serve as reference and for fixation. For LFP recordings, 75 µm teflon-coated tungsten wire (Advent) electrodes were implanted ipsi-unilaterally in the anterior cingulate cortex (Cg, AP: +1.95 mm; L: -0.30, DV: -1.40 mm from brain surface) and retrosplenial cortex (RSA, AP: -2.95 mm; L: -0.4 mm, DV: -0.25

mm from brain surface) according to the Paxinos mouse brain atlas (Paxinos and Watson, 2011). An additional 50 µm stainless steel-coated electrode (A-M Systems) was implanted in the dorsal neck muscle for EMG recording. A 0.1 mm bare silver wire was affixed to the anterior stainless steel crew and used as ground. All the wires were independently joined to a 4 pins connector and fixed on the skull using dental acrylic (DuraLay Reliance). During recovery from surgery mice were supplemented with Carprofen, 5mg/Kg to control pain and inflammations. All mice were allowed to recover for at least 10 days before any test was performed.

LFP recordings were carried out under halothane sedation to reproduce the conditions of rsfMRI imaging. Given the lower susceptibility of LFP to motion contamination, we streamlined animal preparation by delivering the anesthetic via a cone mask. The halothane dose was adjusted to induce sedation, resulting in nominal dosing of 0.7%-1%. LFP signals from mPFC and RSA were recorded for 10 min, sampled at 1600 Hz (bandpass filter 1-700 Hz) and amplified (gain 1000x) through a headstage and a differential pre-amplifier (Omniplex, Plexon). At the end of the experiment, a small electrolytic lesion was made around the tip of the electrode (0.4 mA, 3 s; Cibertec S.A stimulator) before animal perfusion. Serial coronal sections (40 µm) were cut on a vibratome and visualized under the microscope to verify the electrode placement. To investigate the presence of desynchronization at low-frequency bands, 10 min LFP recording bins were band-pass filtered (0.5-40 Hz), downsampled to 256 Hz and detrended using Spike2 customized scripts. To assess synchrony between LFP signals, coherence was calculated via the multi-taper method, using a 200 ms window, time-bandwidth product (TW) of 5 and 9 tapers using the Chronux toolbox (Bokil *et al.*, 2010). LFP signals were empirically binned according to frequency bands: delta (0.5-4 Hz),

theta (4.5-8 Hz), alpha (8-13 Hz), beta (13-25 Hz). Statistical comparisons were carried out using a 2-way ANOVA with repeated measurements.

Retrograde Viral Tracing with Rabies Virus

Unpseudotyped recombinant SADΔG-mCherry rabies virus (RV) was produced as described by Osakada and Callaway (2013). Briefly, B7GG packaging cells, which express the rabies envelope G protein, were infected with unpseudotyped SADΔG-mCherry-RV, obtained by courtesy of Prof. Edward Callaway from the Salk Institute. After five to six days, the virus was collected, filtrated with 0.45 µm filter and concentrated by two rounds of ultracentrifugation. The titer of the SADΔG-mCherry-RV preparation was established by infecting Hek-293T cells (ATCC cat n° CRL-11268) with tenfold serial dilution of viral stock, counting mCherry expressing cells 3 days after infection. The titer was calculated as $2x10^{11}$ Infective Units (IU)/ml, and the stock was therefore considered suitable for in vivo microinjection. Intracortical rabies virus injections were carried out as previously described (Sforazzini *et al.*, 2014a) in adult (12-16 week-old) male 16p11.2$^{+/-}$ and control *16p11.2*$^{+/+}$ littermates (*n* = 6, each group). To this purpose, mice were deeply anesthetized with isoflurane (5%) and firmly stabilized on a stereotaxic apparatus (Stoelting Inc.). A micro drill (Cellpoint Scientific Inc.) was used to drill holes through the skull. Injections were performed with a Nanofil syringe mounted on an UltraMicroPump UMP3 with a four channel Micro4 controller (World Precision Instruments), at a speed of 5 nl/s, followed by a 5–10 minutes waiting period, to avoid backflow of viral solution and unspecific labelling. One µl of viral stock solution was injected unilaterally in the left anterior prefrontal cortex using the following coordinates for injections, expressed in mm from bregma: +1.42 from anterior to posterior, -0.3 lateral, -1.4 depth (Paxinos and Franklin, 2011)

Quantification of Retrogradely Labelled Cells

RV-labelled cell quantification and histological analyses where carried out by an operator (A.B.) blind to genotype as recently described (Liska *et al.*, 2017). After 7 days from viral injection, the animals were transcardially perfused with 4% paraformaldehyde (PFA), brains were dissected, post-fixed over night at 4°C and vibratome-cut (Leica Microsystems). RV-infected cells were detected by means of immunohistochemistry performed on every other 100 µm thick coronal section, using rabbit anti-red fluorescent protein (RFP) primary antibody (1:500, AbCam), and goat anti-rabbit HRP secondary antibody (1:500, Jackson ImmunoResearch), followed by 3-3' diaminobenzidine tetrahydrochloride (DAB, Sigma Aldrich) staining. Imaging was performed with MacroFluo microscope (Leica). Each picture was then superimposed onto the corresponding Paxinos Atlas table (Paxinos and Franklin, 2011), and cell bodies were plotted according to their anatomical localization. The cells were then assigned to their corresponding brain regions, and final region-based cell population counts were expressed as fraction of the total amount of labelled cells.

Dendritic Spine Analysis

Experiments were performed on adult control and 16p11.2$^{+/-}$ mice (n = 8, each group). We quantified the density of dendritic spines in the anterior cingulate cortex (Cg1, AP, +1.34, L, 0.2, D, 0.8) and somatosensory cortex (S1BF, AP, -0.82, L, 3.0, D, 1.5) using the Golgi-Cox staining method as recently described (Martino *et al.*, 2013). Briefly, brains were immersed in the Golgi–Cox solution (1% Potassium Chromate, 1% Potassium Bichromate and 1% Mercury Chloride) for 14 days under dark conditions, and subsequently transferred into a 30% (wt/vol) sucrose solution, in which they were kept for 24 hours. Coronal 100 µm thick sections were collected on X-tra glass slides (Leica), and the staining was developed using a Kodak developer. Slices were then washed with

distilled water, dehydrated, and cleared in successive baths of 50%, 65%, 75%, and 85% (vol/vol) alcohol, and mounted in Eukitt (Sigma-Aldrich).

Z-stack images were acquired with a Nikon microscope using a 100× oil objective and Neurolucida software (MicroBrightField, Williston, VT, USA). High resolution images were processed using ImageJ, deconvolved using AutoQuant (Bitplane) and analyzed using a semiautomatic method with Imaris (BitPlane). Spine density was defined as the number of spines on 10 µm of dendritic length. Images were quantified by an operator blind to experimental conditions (M.B.).

Brain Slice Electrophysiology

Slice Preparation

Young adult 16p11.2$^{+/+}$ and 16p11.2$^{+/-}$ mice (12 week old, n = 4 per group) were anesthetized with isofluorane and decapitated, and their brains were transferred to ice-cold dissecting artificial cerebrospinal fluid (aCSF) containing 110 mM choline chloride, 2.5 mM KCl, 1.25 mM NaH_2PO_4, 7 mM $MgSO_4$, 0.5 mM $CaCl_2$, 25 mM $NaHCO_3$, 25 mM D-glucose, 11.6 mM sodium-L-ascorbate, 3.1 mM sodium pyruvate, saturated with 95% O_2 and 5% CO_2. Coronal sections (250 µm thick) were cut using a Vibratome 1000S slicer (Leica, Wetzlar, Germany), then transferred to aCSF containing 115 mM NaCl, 3.5 mM KCl, 1.2 mM NaH_2PO_4, 1.3 mM $MgCl_2$, 2 mM $CaCl_2$, 25 mM $NaHCO_3$, and 25 mM D-glucose and aerated with 95% O_2 and 5% CO_2. Following 20 min of incubation at 32 °C, slices were kept at 22–24 °C. During experiments, slices were continuously superfused with aCSF at a rate of 2 ml/min at 28 °C.

Whole-cell patch-clamp recordings were made on pyramidal neurons of the layer V of the anterior cingulate cortex. Intracellular solution contained (in mM): 130 $CeMeSO_3$, 5 CsCl, 5 NaCl, 10 HEPES, 0.1 EGTA, 2 $MgCl_2$, 0.05 $CaCl_2$, 2 Na_2-ATP, 0.4 Na_3-GTP (pH 7.2-

7.3, 280-290 mOsm/kg). Patch-clamp pipettes were pulled from borosilicate glass (1.5 mm OD, 0.86 mm ID, 7.5 mm length; Warner Instruments) with a P-97 puller (Sutter Instrument) and had open tip resistances of 4-5 MΩ. Whole cell voltage-clamp recordings were made using a Multiclamp 700B amplifier (Axon Instruments), and neurons were clamped at -70 mV. Spontaneous excitatory post-synaptic currents (sEPSCs) were recorded in presence of 10 μM Gabazine. For miniature EPSCs (mEPSCs), recordings were made also in presence of 1 μM TTX. TTX was perfused for at least 8 minutes before recording. Cells were accepted if access resistances (10-25 MΩ) did not change more than ±20%. Events were analyzed using Minianalysis software (Synaptosoft). EPSCs were detected using a threshold-crossing algorithm, and their frequency, amplitude, and kinetic parameters were analyzed. A Mann-Whitney test was used for comparison of EPSC frequency, amplitude, and kinetic parameters. Values are indicated as mean ± SE.

Electron Microscopy

For conventional electron microscopy, adult 16p11.2$^{+/-}$ (n=4) and control (n=3) mice were perfused transcardially with phosphate buffer (PB 0.1M, pH 7.4) followed by 2% paraformaldehyde and 2% glutaraldehyde in PB. Brains were post-fixed overnight at 4°C in the same fixative. Vibratome sections (200-400 μm thick) were cut sagitally across the corpus callosum (approximately AP, -1.58, L, 2.0) to transect axons perpendicularly to their main longitudinal axis, and post-fixed with 1% osmium tetroxide (OsO4) for 1h at 4°C, then stained with 4x uranyl acetate replacement (UAR Stain). After dehydration in a graded ethanol series, samples were cleared in propylene oxide and embedded in Araldite (Sigma). Semithin sections (1 μm thick) were obtained at the ultramicrotome (Ultracut UCT, Leica, Wetzlar, Germany), stained with 1% toluidine blue and 2% borate in distilled water and then observed under a light microscope for precise location.

Ultrathin sections (70-100 nm) were analyzed with a transmission electron microscope (JEOL, JEM-1010, Tokyo, Japan) equipped with a Mega-View-III digital camera and a Soft-Imaging-System (SIS, Münster, Germany) for computerized acquisition of the images. G-ratio was determined by dividing axon diameter by the total diameter of the axon plus the overlying myelin sheath. Axon diameter was calculated from measured axon perimeter based on an assumption of circularity. All measurements were performed using Image J software on > 50-90 callosal axons per animal. For analyses of the proportion of axons myelinated and g-ratio, at least 50 axons per animal were analyzed.

Supplemental References

Behzadi Y, Restom K, Liau J, Liu TT. A component based noise correction method (CompCor) for BOLD and perfusion based fMRI. NeuroImage 2007; 37(1): 90-101.

Bokil H, Andrews P, Kulkarni JE, Mehta S, Mitra PP. Chronux: A platform for analyzing neural signals. Journal of Neuroscience Methods 2010; 192(1): 146-51.

Carlén M. What constitutes the prefrontal cortex? Science 2017; 358(6362): 478-82.

Chang YS, Owen JP, Pojman NJ, Thieu T, Bukshpun P, Wakahiro ML*, et al.* Reciprocal white matter alterations due to 16p11. 2 chromosomal deletions versus duplications. Human brain mapping 2016; 37(8): 2833-48.

Di Martino A, Yan CG, Li Q, Denio E, Castellanos FX, Alaerts K*, et al.* The autism brain imaging data exchange: towards a large-scale evaluation of the intrinsic brain architecture in autism. Mol Psychiatry 2013.

Dodero L, Damiano M, Galbusera A, Bifone A, Tsaftsaris SA, Scattoni ML*, et al.* Neuroimaging Evidence of Major Morpho-Anatomical and Functional Abnormalities in the BTBR T+TF/J Mouse Model of Autism. PLoS ONE 2013; 8(10): e76655.

Farrell JA, Landman BA, Jones CK, Smith SA, Prince JL, van Zijl PC*, et al.* Effects of signal-to-noise ratio on the accuracy and reproducibility of diffusion tensor imaging-derived fractional anisotropy, mean diffusivity, and principal eigenvector measurements at 1.5 T. J Magn Reson Imaging 2007; 26(3): 756-67.

Ferrari L, Turrini G, Crestan V, Bertani S, Cristofori P, Bifone A*, et al.* A robust experimental protocol for pharmacological fMRI in rats and mice. Journal of Neuroscience Methods 2012; 204(1): 9-18.

Garyfallidis E, Brett M, Amirbekian B, Rokem A, Van Der Walt S, Descoteaux M*, et al.* Dipy, a library for the analysis of diffusion MRI data. Frontiers in Neuroinformatics 2014; 8.

Lerch JP, Pruessner J, Zijdenbos AP, Collins DL, Teipel SJ, Hampel H*, et al.* Automated cortical thickness measurements from MRI can accurately separate Alzheimer's patients from normal elderly controls. Neurobiol Aging 2008; 29(1): 23-30.

Liska A, Bertero A, Gomolka R, Sabbioni M, Galbusera A, Barsotti N*, et al.* Homozygous loss of autism-risk gene CNTNAP2 results in reduced local and long-range prefrontal functional connectivity. Cereb Cortex 2017; 10: 1.

Liska A, Galbusera A, Schwarz AJ, Gozzi A. Functional connectivity hubs of the mouse brain. NeuroImage 2015; 115(0): 281-91.

Liu X, Zhu XH, Zhang Y, Chen W. Neural origin of spontaneous hemodynamic fluctuations in rats under burst-suppression anesthesia condition. Cereb Cortex 2011; 21(2): 374-84.

Martino A, Ettorre M, Musilli M, Lorenzetto E, Buffelli M, Diana G. Rho GTPase-dependent plasticity of dendritic spines in the adult brain. Front Cell Neurosci 2013; 7: 62.

Oguz I, Zhang H, Rumple A, Sonka M. RATS: Rapid Automatic Tissue Segmentation in rodent brain MRI. Journal of Neuroscience Methods 2014; 221: 175-82.

Osakada F, Callaway EM. Design and generation of recombinant rabies virus vectors. Nature protocols 2013; 8(8): 1583-601.

Paxinos G, Franklin K. The Mouse Brain in Stereotaxic Coordinates. 1 ed. Sydney: Academic Press; 2011.

Power JD, Barnes KA, Snyder AZ, Schlaggar BL, Petersen SE. Spurious but systematic correlations in functional connectivity MRI networks arise from subject motion. NeuroImage 2012; 59(3): 2142-54.

Ripley B. MASS: Support functions and datasets for Venables and Ripley's MASS. R package version 7.3-40. 2015.

Sforazzini F, Bertero A, Dodero L, David G, Galbusera A, Scattoni M*, et al.* Altered functional connectivity networks in acallosal and socially impaired BTBR mice. Brain Struct Funct 2014a: 1-14.

Sforazzini F, Schwarz AJ, Galbusera A, Bifone A, Gozzi A. Distributed BOLD and CBV-weighted resting-state networks in the mouse brain. NeuroImage 2014b; 87: 403-15.

Simons VIP Consortium. Simons Variation in Individuals Project (Simons VIP): a genetics-first approach to studying autism spectrum and related neurodevelopmental disorders. Neuron 2012; 73(6): 1063-7.

Steffey MA, Brosnan RJ, Steffey EP. Assessment of halothane and sevoflurane anesthesia in spontaneously breathing rats. American Journal of Veterinary Research 2003; 64(4): 470-4.

Tournier JD, Calamante F, Connelly A. Robust determination of the fibre orientation distribution in diffusion MRI: Non-negativity constrained super-resolved spherical deconvolution. NeuroImage 2007; 35(4): 1459-72.

Tournier JD, Calamante F, Connelly A. MRtrix: Diffusion tractography in crossing fiber regions. International Journal of Imaging Systems and Technology 2012; 22(1): 53-66.

Vogt B, Paxinos G. Cytoarchitecture of mouse and rat cingulate cortex with human homologies. Brain Struct Funct 2014; 219(1): 185-92.

Yushkevich PA, Piven J, Hazlett HC, Smith RG, Ho S, Gee JC*, et al.* User-guided 3D active contour segmentation of anatomical structures: Significantly improved efficiency and reliability. NeuroImage 2006; 31(3): 1116-28.

Zhan Y, Paolicelli R, Sforazzini F, Weinhard L, Bolasco G, Pagani F*, et al.* Deficient neuron-microglia signaling results in impaired functional brain connectivity and social behavior. NatNeurosci 2014; 17: 400-6.